

CO Emission Delineating the Interface between the Milky Way Nuclear Wind Cavity and the Gaseous Disk

YANG SU,¹ SHIYU ZHANG,^{1,2} JI YANG,^{1,2} QING-ZENG YAN,¹ YAN SUN,¹ HONGCHI WANG,^{1,2}
SHAOBO ZHANG,¹ XUEPENG CHEN,^{1,2} ZHIWEI CHEN,¹ XIN ZHOU,¹ AND LIXIA YUAN¹

¹*Purple Mountain Observatory and Key Laboratory of Radio Astronomy, Chinese Academy of Sciences, 10 Yuanhua Road, Nanjing 210023, China*

²*School of Astronomy and Space Science, University of Science and Technology of China, 96 Jinzhai Road, Hefei 230026, China*

ABSTRACT

Based on the MWISP survey, we study high- z CO emission toward the tangent points, in which the distances of the molecular clouds (MCs) are well determined. In the region of $l = 12^\circ\text{--}26^\circ$ and $|b| \lesssim 5^\circ.1$, a total of 321 MCs with $|z| \gtrsim 110$ pc are identified, of which nearly 30 extreme high- z MCs (EHMCs at $|z| \gtrsim 260$ pc) are concentrated in a narrow region of $R_{\text{GC}} \sim 2.6\text{--}3.1$ kpc. The EHMC concentrations, together with other high- z MCs at $R_{\text{GC}} \lesssim 2.3\text{--}2.6$ kpc, constitute molecular crater-wall structures surrounding the edges of the HI voids that are physically associated with the Fermi bubbles. Intriguingly, some large high- z MCs, which lie in the crater walls above and below the Galactic plane, show cometary structures with the head toward the plane, favouring the scenario that the entrained molecular gas moves with the multiphase flows from the plane to the high- z regions. We suggest that the Milky Way nuclear wind has a significant impact on the Galactic gaseous disk. The powerful nuclear wind at $\sim 3\text{--}6$ Myr ago is likely responsible for the observational features: (1) the enhanced CO gas lying in the edges of the HI voids, (2) the deficiency of atomic and molecular gas within $R_{\text{GC}} \lesssim 3$ kpc, (3) the possible connection between the EHMC concentrations and the 3-kpc arm, and (4) the elongated high- z MCs with the tail pointing away from the Galactic plane.

Keywords: Interstellar medium (847); Molecular clouds (1072); Galactic winds (572); Milky Way disk (1050); Interstellar dynamics (839); Stellar feedback (1602)

1. INTRODUCTION

Galactic nuclear outflows and winds, which are powered by energetic processes in the central regions of galaxies, have dominated the transfer of mass, energy, momentum, and metals from the disk to the halo and even the intergalactic medium (IGM). The feedback from the nuclear activity is also crucial for the formation and evolution of galaxies and the IGM (e.g., [Veilleux et al. 2005](#); [Holt et al. 2008](#); [Richings & Faucher-Giguère 2018](#); [Morganti et al. 2021](#)).

The Galactic center (GC) is the nearest laboratory to study the details of the feedback effects from the nuclear region of a galaxy. Over the past several decades, a large number of exciting findings on the multiphase outflows from the GC have been revealed based on the compelling multiwavelength observations of the ground-based telescopes (e.g., Sofue & Handa 1984; Carretti et al. 2013; Hsieh et al. 2016; Heywood et al. 2019; Krishnarao et al. 2020) and the space observatories (e.g., Sofue 2000; Bland-Hawthorn & Cohen 2003; Keeney et al. 2006; Su et al. 2010; Kataoka et al. 2013; Ackermann et al. 2014; Fox et al. 2015; Bordoloi et al. 2017; Predehl et al. 2020). The various studies show that past energetic events (e.g., AGN-driven and/or starburst-driven winds) at about several to tens of Myr ago may be responsible for the nuclear outflow/wind phenomena and the related large-scale structures (see, e.g., the recent reviews by Veilleux et al. 2020; Ponti et al. 2021).

The above studies mainly focus on the radio continuum, IR dust, optical, X-ray, γ -ray emission, and some UV absorption lines on the outflow structures of the Milky Way. On the other hand, the traditional tracers of the neutral atomic and molecular gas (i.e., 21 cm HI and 2.6 mm CO emission) should be also very useful for revealing the spatial and dynamical features of the Galactic nuclear wind on a large scale. In fact, the absence of high- z atomic gas within the inner disk (i.e., Galactocentric distance of $R_{GC} \lesssim 3$ kpc) has been found by Lockman (1984) according to the atomic gas distribution. The molecular gas in the inner 3 kpc of the Galactic disk is deficient with respect to that in the $R_{GC} \gtrsim 3$ kpc region based on the early CO observations and the MWISP data (e.g., Burton et al. 1975; Burton & Gordon 1977; Dame et al. 2001; Su et al. 2021). These results are consistent with the results from the large-scale HI and CO surveys (see, e.g., reviews of Burton 1976; Dickey & Lockman 1990; Combes 1991; Burton et al. 1992; Dame et al. 2001; Kalberla & Kerp 2009; Heyer & Dame 2015).

Moreover, HI study displays a good correlation between the HI voids and the Fermi bubbles, indicating the physical connection between them (Lockman & McClure-Griffiths 2016). Benefiting from the large-scale HI surveys, further studies show that the kinematic features of the atomic gas are very likely related to the Milky Way nuclear wind (e.g., McClure-Griffiths et al. 2009, 2013; Lockman & McClure-Griffiths 2016; Di Teodoro et al. 2018; Lockman et al. 2020; Di Teodoro et al. 2020). Some authors also suggest that the large-scale multiwavelength features can be explained by the interaction between the Galactic nuclear wind (i.e., the GC superbubbles) and the Galactic gaseous disk (e.g., Sofue 2017; Sofue & Kataoka 2021).

In this paper, we present the result of high dynamic range CO observations toward the large-scale view of the inner Galaxy. The kinematic information of the gas allows us to construct the needed molecular cloud (MC) samples from the CO emission, which is very helpful to trace the structures of the gaseous disk of the Milky Way. At $\gtrsim 260$ pc (and even $\gtrsim 600$ pc) above and below the Galactic plane, the enhanced CO emission is discovered to be concentrated in a narrow range of $l \sim 18^\circ - 22^\circ$ or $R_{GC} \sim 2.6-3.1$ kpc for the Sun's distance to the GC of $R_0=8.15$ kpc (e.g., Reid et al. 2019), indicating the interface between the Milky Way nuclear wind and the gaseous disk. Furthermore, some cometary CO structures exhibiting the head toward the Galactic plane and the tail away from the plane show that the cold molecular gas is entrained in multiphase flows. The multiphase outflows are probably driven by the warm/hot gas from the Milky Way nuclear wind.

In Section 2, we describe the CO, HI, and IR data used in the paper. In Section 3, we discuss the results and then give a simplified picture to explain the multiwavelength observations. Finally, Section 4 gives a brief summary based on our new findings.

2. CO, HI, AND IR DATA

The CO data are from the Milky Way Imaging Scroll Painting survey (i.e., the MWISP project; see details in [Su et al. 2019](#)). Briefly, we employed the CO emission in the region of $l = 12^\circ\text{--}26^\circ$ and $|b| \lesssim 5^\circ.1$ to investigate the molecular gas distribution near the tangent points, where the gas's distance is well determined. The spatial and spectral resolutions of the CO data are $\sim 50''$ and $\sim 0.2 \text{ km s}^{-1}$, respectively. After fitting the baseline and calibrating the main-beam efficiency, the reduced 3D data cubes (i.e., the position-position-velocity space, hereafter PPV) with a grid spacing of $30''$ have a typical rms noise level of $\sim 0.5 \text{ K}$ for ^{12}CO ($J=1\text{--}0$) and $\sim 0.3 \text{ K}$ for $^{13}\text{CO}/\text{C}^{18}\text{O}$ ($J=1\text{--}0$) at a channel width of 0.16 km s^{-1} . We mainly focus on the ^{12}CO ($J=1\text{--}0$) emission in this paper.

In this work, the HI data from the all-sky HI survey ([HI4PI Collaboration et al. 2016](#)) are used for large-scale comparisons with the MWISP CO data. The angular and velocity resolutions of the HI data are $16''.2$ and 1.5 km s^{-1} , respectively. The typical RMS sensitivity of the HI4PI data is $\sim 43 \text{ mK}$. We also use the data from the survey of the Wide-field Infrared Survey Explorer ([WISE; Wright et al. 2010](#)) to investigate the correlation between the molecular gas distribution and the dust emission. The $12 \mu\text{m}$ and $22 \mu\text{m}$ WISE data used here have a spatial resolution of $6''.5$ and $12''.0$, respectively.

3. RESULTS AND DISCUSSIONS

3.1. *Thinner Gaseous Disk within $R_{\text{GC}} < 3 \text{ kpc}$*

The HI data have shown that the atomic gas layer is noticeably thin in the region of $R_{\text{GC}} \lesssim 3 \text{ kpc}$, probably indicating the interaction between the Milky Way nuclear wind and the gaseous disk ([Lockman 1984; Lockman & McClure-Griffiths 2016](#)). And the early CO observations also show that the cold compressed gas is confined to a thinner layer within $R_{\text{GC}} < 3 \text{ kpc}$ (e.g., [Burton et al. 1975; Burton 1976; Burton & Gordon 1977](#)). Recently, a large number of small and high-velocity HI clouds are found to be far above and below the disk toward the GC, suggesting that the large-scale atomic gas is physically associated with the Fermi bubbles and then the Milky Way nuclear wind ([McClure-Griffiths et al. 2013; Di Teodoro et al. 2018; Lockman et al. 2020](#)).

Furthermore, [Di Teodoro et al. \(2020\)](#) have revealed that the cold and dense molecular gas far from the plane can even survive in the hot and shocked nuclear wind. These results show that energetic processes in the GC have profound effects on the distribution and evolution of the interstellar medium (ISM) on a large scale, which is consistent with the observational and theoretical studies on other galaxies (see the summary in [Veilleux et al. 2020](#)).

As a widely used tracer of the MCs, CO data can provide the large-scale spatial and kinematic information of the H_2 gas. In this study, we explore the distribution and properties of the molecular gas far from the Galactic plane based on the MWISP CO data. The study is limited to the CO emission near the tangent points, which can avoid the distance ambiguity and thus decrease the foreground confusion of the unrelated structures (see, e.g., the schematic view of Figure 1 in [Su et al. 2021](#)).

We have confirmed that the inner molecular disk consists of two components: the thin CO layer with a thickness of $\sim 85 \text{ pc}$ and the thick layer with $\sim 280 \text{ pc}$ ([Su et al. 2021](#)). The well-known thin CO disk harbors the majority of the molecular gas in the Milky Way, while the thick CO disk is composed of many small clouds in relatively high- z regions. Some MCs in the thick CO layer are

probably related to the feedback of the energetic star-forming activities near the Galactic plane (see, e.g., the case of microquasar SS 433 in [Su et al. 2018](#)). Interestingly, the two molecular gas layers are both thinner within the $R_{GC} \lesssim 3$ kpc region (i.e., an FWHM of ~ 60 pc and ~ 150 pc for the thin and thick CO layers, respectively; see Figures 3-5 in [Su et al. 2021](#)).

Figure 1 shows a large-scale distribution of the atomic and molecular gas toward the tangent points. That is, we just integrated the gas emission with velocities greater than the terminal velocities. Here the terminal velocities can be determined from the most positive velocity of the CO emission in the first quadrant of the Milky Way (see details in [Su et al. 2021](#)). Obviously, the disk traced by the atomic and molecular gas is indeed thinner in regions of $l \lesssim 22^\circ$ (or $R_{GC} \lesssim 3$ kpc).

Is the thinner gaseous disk within $R_{GC} \lesssim 3$ kpc related to the large-scale H I voids or the Milky Way nuclear wind? Is a substantial amount of cold neutral gas entrained by the Milky Way nuclear wind? If so, why is the neutral gas not destroyed by the high-velocity wind in such harsh environments? And what is the relation between the cool outflows and the hot wind from the nuclear region of the Milky Way? The MWISP CO data with a wide spatial dynamic range, in combination with H I and other multiwavelength observations, can give some hints on these topics.

3.2. Enhanced high- z CO Emission toward $l \sim 19.1-22.5$

MCs far from the Galactic plane may reveal some features of the large-scale structures related to the Milky Way nuclear wind. To search for the high- z MCs in the MWISP 3D datacube, we use the density-based spatial clustering of applications with noise (DBSCAN¹) clustering algorithm. The algorithm is useful to identify CO clouds with noise in a big dataset, which is crucial to reveal possible unusual features traced by weak emission. Full details of the algorithm can be found in our previous studies (e.g., [Yan et al. 2020](#); [Su et al. 2021](#)), and a brief description of the method is shown below.

In order to further improve the signal-to-noise ratio, the MWISP raw data were resampled to 0.5 km s^{-1} , corresponding to a typical rms noise level of ~ 0.3 K per channel for the ^{12}CO emission. For the PPV space, the minimum cutoff is $2 \times \text{rms}$ and MinPts is set to 4 in the DBSCAN algorithm. Then, post-selection criteria (i.e., $T_{\text{peak}} \geq 4 \times \text{rms}$, $\Delta l \times \Delta b \geq 1$ beam, $\Delta v \geq 3$ channels, and the minimum number of neighborhood voxels ≥ 16) are used on the samples to remove the noise contamination. Here T_{peak} is the intensity per channel in the units of K, Δl (Δb) is the spatial size in the units of arcmin, and Δv is the spectral extension in the units of km s^{-1} . Note that we use $T_{\text{peak}} \geq 4 \times \text{rms}$ as the post-selection criteria, which allows us to detect weaker CO emission in the whole data compared to our previous studies (e.g., $T_{\text{peak}} \geq 5 \times \text{rms}$ in [Su et al. 2021](#)).

Furthermore, we identified the high- z MCs toward the tangent points according to the selection criteria of $v_{\text{MC}} \gtrsim v_{\text{tan}}(l) - 7 \text{ km s}^{-1}$ and $|z_{\text{MC}}(l, b, v)| \geq 110 \text{ pc}$ (i.e., $\geq 3 \times \sigma_z$ of the thin CO disk; see Table 3 in [Su et al. 2021](#)). Here v_{MC} and $v_{\text{tan}}(l)$ are the velocity of the MC and the corresponding tangent velocity at a certain longitude, respectively. And σ_z is the standard deviation of the vertical distribution of the CO emission. By considering the cloud-cloud velocity dispersion of MCs ([Malhotra 1994](#); [Su et al. 2021](#)), we adopted the value of $v_{\text{tan}}(l) - 7 \text{ km s}^{-1}$ to build the high- z MC samples near the tangent points.

To reduce striping artifacts and other uncertainties in the whole data, all selected MC samples are manually checked based on the cloud's spatial and velocity features in the PPV space. We find that the procedure is efficient and valid. The method with the improved criteria can substantially increase

¹ https://scikit-learn.org/stable/auto_examples/cluster/plot_dbscan.html

the MC samples with weak CO emission, which is important to reveal the molecular gas distribution traced by small and faint clouds at the marginal signal-to-noise ratio of the MWISP survey. And some interesting structures with weaker CO emission are indeed revealed in our subsequent analysis (e.g., small MCs with $T_{\text{peak}} \sim 1$ K, see Section 3.3).

In total, 321 MCs near the tangent points were identified as the high- z MC samples (i.e., $|z| \gtrsim 110$ pc) in the region of $l = 12^\circ\text{--}26^\circ$ and $|b| \lesssim 5^\circ.1$ (see purple circles in Figure 1). These discrete high- z MCs usually have small sizes ($\sim 0.7\text{--}2.2$ or $\sim 1\text{--}5$ pc in the radius), weak emission ($\sim 1\text{--}3$ K in the peak temperature), and high virial parameters ($\sim 5\text{--}30$), which are consistent with our previous studies (e.g., Su et al. 2021).

Obviously, the high- z MCs are well coincident with the distribution of the HI emission near the tangent points, indicating the physical association between them (Figure 1). We check the spectral properties between the high- z CO cloud and the HI gas at the same location. Both the CO cloud and the HI gas have comparable LSR velocity near the tangent points, confirming the association of them.

Figure 2 displays the 321 high- z MCs in the $R_{\text{GC}}\text{--}z$ space. Besides the thinner gas layers discussed in Section 3.1, interestingly enough, we also found that the extreme high- z MCs (hereafter EHMCs) are located in two NARROW regions of [$l \sim 19^\circ.1$ to $20^\circ.5$, $b \sim 2^\circ.0$ to $5^\circ.1$] and [$l \sim 20^\circ.5$ to $22^\circ.1$, $b \sim -2^\circ.0$ to $-5^\circ.1$] (see Figures 1 and 2). These EHMCs (i.e., $|z| \gtrsim 260$ pc or $\sim 3 \times \text{FWHM}$ of the thin CO layer) are unusual in such the narrow region far above and below the Galactic plane. The molecular gas mass of the EHMCs is also concentrated in the narrow range of $R_{\text{GC}} = 2.6\text{--}3.1$ kpc (i.e., $\gtrsim 9.2 \times 10^3 M_\odot$ in regions of $\sim 2 \times \Delta R_{\text{GC}} \times \Delta z = 2 \times 220 \text{ pc} \times 410 \text{ pc}$, see the histogram in Figure 2 and Section 3.3).

These EHMCs, together with other high- z MCs at $R_{\text{GC}} \lesssim 2.3\text{--}2.6$ kpc, constitute molecular crater-wall structures lying along the edges of the HI voids (i.e., from $l \sim 17^\circ$ and $|b| \gtrsim 1^\circ$ to $l \sim 22^\circ$ and $|b| \gtrsim 5^\circ$, see Figure 1). We suggest that the molecular crater walls, in combination with the HI voids above and below the Galactic plane, are related to the GC superbubbles seen in radio, X-ray, and γ -ray emission (e.g., Fermi bubbles; Su et al. 2010).

3.3. EHMCs and Cometary Structures

Table 1 lists the parameters of each EHMC: (1) the ID of the EHMCs, arranged from the low Galactic longitude; (2) and (3) the EHMC's Galactic coordinates (l and b); (4) the EHMC's LSR velocity (v_{LSR}); (5) the EHMC's one-dimensional velocity dispersion (σ_v); (6) the EHMC's peak emission (T_{peak}); (7) the EHMC's effective radius (i.e., $d \times \sqrt{(\theta_{\text{MC}}^2 - \theta_{\text{beam}}^2)}/\pi$, where θ_{MC} and θ_{beam} , in units of arcmin, are the angular size of the CO emission and the beam size, respectively); (8) the EHMC's distance obtained from the tangent points, i.e., $d = 8.15 \text{ kpc} \times \cos(l)/\cos(b)$; (9) the EHMC's z height defined as $z = d \times \sin(b)$; (10) the EHMC's mass estimated from the CO-to- H_2 conversion factor method, $X_{\text{CO}} = 2 \times 10^{20} \text{ cm}^{-2} (\text{K km s}^{-1})^{-1}$ (e.g., Dame et al. 2001; Bolatto et al. 2013a); and (11) the EHMC's virial parameter $\alpha = \frac{M_{\text{virial}}}{M_{\text{Xfactor}}} = \frac{5\sigma_v^2 R}{GM_{\text{Xfactor}}}$, where R is the effective radius of the EHMCs and G the gravitational constant.

Generally, the 47 EHMCs also have small sizes of several arcminutes (the mean value of $3'.1$ and the median value of $2'.4$), weak emission (the mean value of 1.6 K and the median value of 1.8 K), and molecular masses spanning $40\text{--}3100 M_\odot$ (the mean value of $340 M_\odot$ and the median value of $110 M_\odot$). Based on the new criteria (Section 3.2), about half of the EHMCs are small clouds with

a mass of $\lesssim 100 M_{\odot}$. As the location anchors, the EHMCs are essential to trace the molecular crater-wall structures located along the edges of the HI voids at $\sim 18^{\circ}$ – 22° (Figure 1).

Moreover, some large EHMCs display spatially resolved structures. Two zoomed-in views of the EHMCs are shown in Figure 3 for EHMC G019.957+02.863 and EHMC G021.548–03.414 (also see regions of the red boxes in Figure 1). Based on the new MWISP CO data at moderately high angular resolution and fairly high sensitivity, we find that the two EHMCs traced by CO emission (black contours) display the elongated head-to-tail structures pointing away from the Galactic plane (see blue arrows in Figure 3). We also find that the elongation of the molecular gas coincides exactly with the atomic gas ridges revealed by HI emission (see purple contours in Figure 3) and the dust filaments traced by IR emission.

Remarkably, the cometary structure of the EHMC G021.548–03.414 can be clearly seen from the CO emission (i.e., see CO black contours of the ~ 20 pc long structure in the bottom panel of Figure 3). The CO emission of the head of the EHMC is brightest toward the Galactic plane, while the cometary tail is faint away from the plane. At the head of the EHMC, the ^{12}CO peak temperature is ~ 4.4 K, which is about four times of the detected ^{13}CO emission at the brightest part of the ^{12}CO emission (i.e., $T_{\text{peak}^{13}} \sim 4 \times \text{rms}^{13} = 1.1$ K, see Table 1). We also show the peak temperature of the detected ^{13}CO emission for the EHMCs in Table 1. No C^{18}O emission is detected for any identified EHMCs.

Contrary to the bright CO emission at the head of the cometary cloud, the IR dust emission is bright in the tail regions where the atomic gas is also enhanced based on the HI data with a grid of $5'$ (Figure 3). The feature probably indicates that the entrained molecular gas (and dust) in the tail is heated by the surrounding warm/hot gas, leading to the multiphase flows from the cold head to the warm tail in the crater-wall region. Based on the WISE data, the dust temperature at the tail of the EHMC G021.548–03.414 is probably ~ 100 – 500 K, which is larger than the molecular gas temperature at the head of the cloud (e.g., the estimated molecular gas temperature of $\lesssim 10$ K based on the optically thick ^{12}CO emission and the beam filling factor of 1). We must stress that the derived dust temperature is dependent on the accurate IR flux from the thermal emission at several bands. More observations are necessary to draw a solid conclusion. On the other hand, there are at least three MC structures (i.e., EHMC ID 13, 14, and 15 in Table 1) concentrated in the region toward EHMC G019.957+02.863.

Figure 4 shows the position–velocity (PV) diagrams of the two EHMCs from the head to the tail (see blue arrows in Figure 3). For EHMC G021.548–03.414, the velocity gradient of $\sim -0.23 \text{ km s}^{-1} \text{ pc}^{-1}$ is found to be from the denser head to the faint tail. Considering a small inclination angle of $i \sim 10^{\circ}$ – 20° for the outflows on the sky, the true velocity gradient could be larger (e.g., $\sim -1 \text{ km s}^{-1} \text{ pc}^{-1}$ for the moving flows roughly perpendicular to the line of sight). The entrained molecular gas of the EHMC is moving toward us based on the observed blueshifted CO emission.

These new findings indicate that the head of the high- z MCs mainly contains cold and dense molecular gas, while the extended filamentary tail incorporates a substantial amount of atomic gas, molecular gas, and dust stripping from the MC's head. That is, the molecular gas is changing phase to become the atomic gas (and very likely the warm ionized gas) as it moves to the high- z regions. The material in the tail is comoving with the surrounding warm/hot ionized gas from the low- z regions to the high- z regions, providing a supply of fresh gas to the Milky Way halo and eventually

falling back onto the plane (e.g., the velocity of cool outflows at $\sim 140 - 330 \text{ km s}^{-1}$ is less than the escape velocity of the Milky Way; see Section 3.4.2).

The association of the bright dust emission with the cool gas in the tail shows that the dust can survive long in the crater walls with the local high density (e.g., at least several Myr; see Section 3.4.3). The survival of dust is very important for efficient formation of molecules in the interface between the cool outflows and the warm/hot wind. The observation features are also consistent with the recent simulation results that the molecular and dusty clouds are likely to survive long enough in warm/hot winds (e.g., Gronke & Oh 2018, 2020; Banda-Barragán et al. 2019; Farber & Gronke 2022).

Some other elongated high- z CO clouds lying in the edges of the H I voids are also shown in Figure 5. We note that the MCs in panels (c) and (d) of Figure 5 form a $\sim 140 \text{ pc}$ long structure from $b \sim -2^\circ.6$ to $b \sim -3^\circ.5$, supporting the existence of the large-scale molecular crater walls along the edges of the H I voids (and the boundary of the GC superbubbles; see Figure 6).

3.4. Impact of Galactic Winds on the Gaseous Disk

3.4.1. Origin of the EHMCs

There are probably two scenarios that can explain the observed EHMCs far from the Galactic plane, i.e., (1) the local star-formation-feedback scenario and (2) the Milky Way nuclear wind scenario. We will discuss the two scenarios described below.

For the local star formation feedback scenario, the feedback from star-forming activities near the Galactic plane has profound effects on the surrounding ISM environment, i.e., changing the physical properties and the distributions of the gas. The energetic processes from massive stellar winds and/or supernova explosions can produce large-scale structures such as supershells, superbubbles, and large-scale chimneys. Especially, the region between $l \sim 20^\circ$ and 30° is close to the near tip of the Galactic bar and it hosts intense star-forming regions in the Galactic plane. The region also shows a rich population of H I extraplanar clouds that are not seen in other regions of the Galaxy (the H I scale height in the region of $l \sim 20^\circ$ is twice the scale height of the corresponding region in $l \sim -20^\circ$, see Ford et al. 2008, 2010)

Therefore, the high- z MCs ($|z| \gtrsim 100 \text{ pc}$) in the thick CO disk may be the debris of the disk gas that was blown away by local star-formation feedback near the Galactic plane (see, e.g., discussions in Su et al. 2021). For example, the identified high- z MCs at ($l \sim 40^\circ.3$, $b \sim -4^\circ.3$) are probably associated with the nearby SS 433/W50 system (e.g., $z_{\text{MC}} \sim -400 \text{ pc}$ at a distance of 5 kpc; see Su et al. 2018). Is it possible that the EHMCs at $l \sim 20^\circ$ are from the energetic processes of stellar feedback near the Galactic plane, for example, the Ophiuchus superbubble (see details in Pidopryhora et al. 2007)?

Based on results from the MWISP data, we find that the high- z MCs with very faint CO emission are highly turbulent, indicating that the cold gas is mixing with the warmer gas and the MCs are either dispersing or being assembled by external dynamical processes. These small-sized (1–4 pc) high- z MCs are probably short-lived, e.g., less than their typical internal crossing time of several Myr. The clouds thus cannot move too far from the disk if they are directly from the Galactic midplane, conforming to the observed MCs' distribution for the thick CO disk (e.g., $\sigma_z \sim 110\text{--}120 \text{ pc}$; see Su et al. 2021). Here we ignore the case that the high- z molecular gas may condense in situ. Indeed, we find no detailed correlation between the Ophiuchus superbubble in H I emission and the

high- z MCs near the tangent point in a region of $l \sim 20^\circ\text{--}40^\circ$ and $z=100\text{--}600$ pc. On the other hand, the Ophiuchus superbubble appears to be one-sided and does not extend below the Galactic plane (e.g., [Pidopryhora et al. 2007](#)), although the HI4PI data show a lot of anomalous structures below the Galactic plane (see also [Ford et al. 2010](#); [Su et al. 2021](#)). We argue that the enhanced EHMCs at $l \sim 18^\circ\text{--}22^\circ$ (or $R_{\text{GC}} \sim 2.6\text{--}3.1$ kpc) are not associated with the old Ophiuchus superbubble (e.g., an age of about 30 Myr; see [Pidopryhora et al. 2007](#)).

In principle, some EHMCs are probably related to the young star-formation feedback (e.g., several Myr) near the Galactic plane. However, the extended direction of the cometary EHMCs (see [Figure 3](#)) and the coherent EHMC samples in [Figure 6](#) show that the large and cometary EHMCs are likely related to dynamical processes toward regions of $l \lesssim 18^\circ\text{--}22^\circ$ (or toward the GC direction), in which the star-forming activities near the Galactic plane are not very intense except for the Central Molecular Zone (CMZ) region.

According to the above discussions, we propose that most of the EHMCs in $R_{\text{GC}} \sim 2.6\text{--}3.1$ kpc are associated with the Milky Way nuclear wind. We also summarize the observation results as below:

- (1) The dominant EHMCs are just located near the edges of the large-scale HI voids toward $l \sim 18^\circ - 22^\circ$ or $R_{\text{GC}} \sim 2.6\text{--}3.1$ kpc (see [Figures 1, 2, and 6](#)), indicating the association between them.
- (2) The large EHMCs along the edges of the HI voids display unusual head-to-tail structures pointing away from the Galactic plane (or the direction away from the GC; see [Figures 3 and 5](#)).
- (3) The observed velocity gradient of EHMC G021.548–3.414, together with its large velocity width ([Figure 4](#)), supports the idea that the MC is unstable and is partially destroyed by ambient dynamical processes. That is, the molecular gas is accelerated from the head to the tail owing to the blueshifted CO profile for the tail structure (see the bottom panel of [Figure 4](#)). The feature supports the entrainment scenario that the material is moving from the Galactic plane to the high- z regions.
- (4) The IR emission of EHMC G021.548–3.414 ([Figure 3](#)) is bright at its long tail but is faint at the dense head, favoring the scenario of the molecular gas being ablated and heated from the cloud edges by a warm/hot wind.

These observational features can be naturally explained by the entrainment scenario that the cold gas is moving with the multiphase medium at the interface between the warm/hot nuclear wind of the Milky Way and the gaseous disk. The process also leads to the concentrated molecular gas (and mass) in narrow regions of $l \sim 18^\circ - 22^\circ$ (or $R_{\text{GC}} \sim 2.6\text{--}3.1$ kpc) and $|z| \gtrsim 260$ pc (see the cometary EHMCs along the edges of the HI voids in [Figures 3 and 6](#), $|z| \sim 400 - 450$ pc $\gtrsim 3\sigma_z$ of the thick CO disk).

The HI voids, which are physically associated with the Fermi bubbles, are thus surrounded by enhanced CO emission at low latitudes of $|b| \gtrsim 2^\circ\text{--}5^\circ$ and $R_{\text{GC}} \lesssim 2.6\text{--}3.1$ kpc. This scenario also agrees well with the recent observation that the Milky Way nuclear wind can remove gas from the disk to the halo (e.g., [Cashman et al. 2021](#)) and can accelerate MC fragments into the high- z regions (e.g., [Di Teodoro et al. 2020](#)).

Finally, note that not all EHMCs in [Table 1](#) are related to the Milky Way nuclear winds. Only samples of ID 05–31 in [Table 1](#) are used to calculate the mass of the crater walls (see [Figure 2](#)). Among the EHMCs in the crater walls, over 60% of samples are resolved and nearly 30% of EHMCs (ID 13, 14, 15, 19, 23, 24, and 27) display cometary structures. These features are unusual in the narrow region of $R_{\text{GC}} \sim 2.6\text{--}3.1$ kpc. And the dominant molecular mass in the CO crater walls is from the large-size and cometary EHMCs that are located along the edges of the HI voids (e.g.,

$R_{\text{GC}} \sim 2.6\text{--}3.1$ kpc; see EHMCs in Figure 6 and the caption). Therefore, the possible contamination from the local star-formation feedback near the Galactic plane has little effect on the subsequent estimation assuming that the cometary and large EHMCs along the crater walls are (very likely) of Milky Way nuclear wind origin.

Of course, observing a similar region at the other side of the crater (i.e., $l \lesssim -20^\circ$), where star-formation activity is not very intense, would be a neat confirmation. However, the MWISP survey cannot cover that longitude range.

3.4.2. Cool Outflows in the Milky Way

Multiphase outflows are a common feature in galaxies (e.g., Veilleux et al. 2020). For the Milky Way, multiwavelength observations have revealed many interesting large-scale structures related to the Galactic nuclear wind, i.e., the GC Lobes in radio (e.g., Sofue & Handa 1984; Carretti et al. 2013), IR (e.g., Bland-Hawthorn & Cohen 2003), X-ray (e.g., Predehl et al. 2020), γ -ray (i.e., the Fermi bubbles in Su et al. 2010) emission and UV absorption (e.g., Zech et al. 2008; Fox et al. 2015; Savage et al. 2017; Karim et al. 2018; Ashley et al. 2020), showing the bipolar outflows on scales of a few degrees to tens of degrees.

New multiwavelength analyses also found chimney-like structures that are physically related to the intermittent activity near the GC (Ponti et al. 2019, 2021). Recently, the HI studies have revealed spatial (e.g., HI holes in Lockman & McClure-Griffiths 2016) and kinematic atomic gas features (e.g., anomalous high-velocity clouds extending up to the high- z regions; McClure-Griffiths et al. 2013; Di Teodoro et al. 2018; Lockman et al. 2020) associated with the Galactic wind. These studies support the existence of large-scale multiphase outflows in our Galaxy (i.e., the neutral gas at $T \lesssim 10^2$ K, warm ionized gas $T \sim 10^3 - 10^4$ K, and high-temperature gas at $T \gtrsim 10^6$ K).

Based on the discussions in Section 3.4.1, we suggest that large amounts of molecular gas, which is concentrated in the edges of the HI voids associated with the Fermi bubbles, is entrained in large-scale multi-phase outflows from the Galactic gaseous disk to the high- z regions.

The detected EHMCs could be an important mass reservoir of the cool outflows in the Milky Way. The molecular mass in the crater-wall structures of $l \sim 19.1\text{--}22.5$ and $|z| \gtrsim 260$ pc (i.e., Area $\sim 2 \times \Delta R_{\text{GC}} \times \Delta z = 2 \times 220$ pc width $\times 410$ pc height; see Figure 2 and ID 05–31 in Table 1) is estimated to be $\gtrsim 9.2 \times 10^3 M_\odot$ by adopting the CO-to-H₂ conversion factor of $X_{\text{CO}} = 2 \times 10^{20} \text{ cm}^{-2} (\text{K km s}^{-1})^{-1}$ (e.g., Dame et al. 2001; Bolatto et al. 2013a). In the meanwhile, many small clouds with weak CO emission (e.g., $T_{\text{peak}} \lesssim 1$ K) may exist in the walls of the crater-like structures, but we cannot pick them out owing to the beam dilution and the limited sensitivity of the survey data. For a conservative estimate, the mean volume density of the molecular gas in the crater walls is $\gtrsim 3 \times 10^{-4} M_\odot \text{ pc}^{-3}$ (or $\gtrsim 0.01 \text{ H cm}^{-3}$) assuming a thickness of ~ 200 pc along the line of sight (LOS).

Due to confusion with the unrelated HI emission near the Galactic plane, the total mass of the atomic gas cannot be precisely measured in the same region of the EHMC concentrations. Based on the HI emission near the tangent points, however, the upper limit of the total mass of the atomic gas can be roughly estimated to be $\lesssim 1.3 \times 10^5 M_\odot$ from $I_{\text{HI}}(v_{\text{LSR}} > v_{\text{tan}})$, leading to the atomic gas density of $\lesssim 4 \times 10^{-3} M_\odot \text{ pc}^{-3}$ (or $\lesssim 0.1 \text{ H cm}^{-3}$). Note that the estimated HI mass contains the attribution from some unrelated gas structures with $v_{\text{LSR}} < v_{\text{tan}}$ because of the broad line width of the HI emission. Therefore, the derived atomic gas mass (and the density) toward the tangent points is probably the upper limit based on the estimated value of $I_{\text{HI}}(v_{\text{LSR}} > v_{\text{tan}})$.

The mean density of the cold gas estimated above is at least one order of magnitude larger than the hot gas density in the bubbles (e.g., the often-used value of $\sim 10^{-3} \text{ H cm}^{-3}$ in Bland-Hawthorn & Cohen 2003; Crocker et al. 2015; Sarkar et al. 2015; Miller & Bregman 2016), suggesting that the hot gas in the nuclear wind is surrounded by dense and cold shells at the boundaries of the Fermi bubbles near the Galactic gaseous disk. Therefore, the cold gas at $R_{\text{GC}} \sim 3 \text{ kpc}$ likely confines the hot wind near the gaseous disk at least on the height of $|z| \sim 600 \text{ pc}$ (see Figures 1 and 2). That is what we observed based on the MWISP CO survey and the combination of the HI data.

Considering the bipolar-outflow structures for the Milky Way nuclear wind, we can estimate that the total mass of the molecular crater walls should be $\gtrsim 1 \times 10^6 M_{\odot}$ for regions of $\sim 2 \times 2\pi R_{\text{GC}} \times \Delta R_{\text{GC}} \times \Delta z = 3.4 \times 10^9 \text{ pc}^3$ (i.e., the two bowl-like structures above and below the Galactic plane at $R_{\text{GC}} \sim 3 \text{ kpc}$ and $|z| \sim 260\text{--}670 \text{ pc}$). It is interesting to note that the total molecular mass in the crater walls is well comparable to that of the HI gas in the Fermi bubbles (i.e., $\sim 10^6 M_{\odot}$ in Di Teodoro et al. 2018; Lockman et al. 2020). Additionally, some molecular gas could still survive in the inner of the Fermi bubbles (e.g., Di Teodoro et al. 2020), which will increase the total molecular mass of the cool outflows associated with the Milky Way nuclear wind.

Our results show that a large amount of neutral gas (the total atomic and molecular gas mass of $\sim 10^7 M_{\odot}$ at $|z| \gtrsim 260 \text{ pc}$) is located in the crater walls, which surround the base of GC superbubbles at low latitudes above and below the Galactic plane. The high- z molecular gas, together with the related atomic gas and dust, constitutes the cool outflows associated with the Milky Way nuclear wind.

Figure 6 shows large-scale velocity distributions of the gas along the crater-wall structures (black dashed lines in the left panel). We find that the crater-wall structures display the systematic velocity gradient of $\sim -0.03 \text{ km s}^{-1} \text{ pc}^{-1}$ along the LOS. That is, the observed velocity along the LOS decreases with increasing the height of $|z|$, for regions both above (e.g., EHMC IDs 5–13 in Table 1) and below (EHMC IDs 19–28 in Table 1) the Galactic plane. The lag is probably the result of the interaction between the entrained gas from the disk and the slowly rotating gas in the halo (e.g., Fraternali & Binney 2008; Melioli et al. 2009; Marasco et al. 2015; Lockman & McClure-Griffiths 2016).

Additionally, two substructures, which are identified from the coherent EHMCs with similar spatial and velocity features in the crater walls, display the positive velocity gradient with increasing the height of $|z|$ (see the black solid lines in the right panels of Figure 6). Here the coherent EHMCs mean that (1) the clouds have similar LSR velocities in a small region and (2) they have similar elongations along the crater walls (or the edges of the HI voids). Both the substructures traced by CO emission are located at $\sim 400\text{--}450 \text{ pc}$ far from the Galactic plane (see, e.g., black contours in Figure 3).

The velocity gradients of the two substructures are $\sim 0.15 \text{ km s}^{-1} \text{ pc}^{-1}$ for the $\sim 20 \text{ pc}$ long structure above the plane (see the black solid line in the top right panel of Figure 6 for EHMCs IDs 13, 14, 15, and 17 from Table 1) and $\sim 0.16 \text{ km s}^{-1} \text{ pc}^{-1}$ for the $\sim 40 \text{ pc}$ long one below the plane (see the black solid line in the bottom right panel of Figure 6 for EHMCs IDs 23, 24, 26, and 27 from Table 1), respectively. The true velocity gradient is likely 3–6 times larger than the observed gradient along the LOS by considering the projection correction of the small inclination angle (e.g., $\nabla v_{\text{true}} = \nabla v_{\text{obs}} / \sin(i)$ for $i \sim 10^{\circ} - 20^{\circ}$; see Section 3.3).

We argue that the velocity gradient of the large-scale coherent EHMCs probably results from cool outflows associated with the Milky Way nuclear wind. The velocity of cool outflows is roughly $\sim 140 - 330 \text{ km s}^{-1}$ (i.e., $v_w \sim path \times \nabla v_{\text{true}}$) assuming that the CO gas comes from the locations of 110–130 pc far from the Galactic plane at a constant acceleration (e.g., $path \sim 280\text{--}330 \text{ pc}$ and $\nabla v_{\text{true}} \sim 0.5 - 1 \text{ km s}^{-1} \text{ pc}^{-1}$). Here we tentatively assume that the entrained high- z gas is launched from the boundary of the thin CO disk to their current places (see, e.g., the cometary CO structures at $b \sim 1^\circ$ or $|z| \sim 120 \text{ pc}$ in the top panels of Figure 5). The estimated velocity of the cool outflows is roughly comparable to the value of $\sim 200\text{--}300 \text{ km s}^{-1}$ from the HI kinematic models (e.g., McClure-Griffiths et al. 2013; Di Teodoro et al. 2018; Lockman et al. 2020).

The cold gas in the multiphase outflows is mainly entrained along the walls of the hot gas cavity blown by the Milky Way nuclear wind. The scenario is also similar to the famous examples of nearby starburst galaxy M82 (e.g., Leroy et al. 2015; Yoshida et al. 2019; Krieger et al. 2021) and NGC 253 (e.g., Bolatto et al. 2013b; Meier et al. 2015; Walter et al. 2017; Krieger et al. 2019). Further observations and simulations are helpful in understanding the whole picture of the Galactic multiphase nuclear outflows/winds (e.g., Fang et al. 2020; Zhang & Guo 2020; Banda-Barragán et al. 2021; Cecil et al. 2021; Pillepich et al. 2021; Mondal et al. 2021; Fielding & Bryan 2022; Tanner & Weaver 2022; Yang et al. 2022).

3.4.3. Survival of Molecular Gas in the High- z Regions

In principle, the isolated and cool clouds (e.g., $n \sim 10\text{--}1000 \text{ cm}^{-3}$ and $T \lesssim 10^2 \text{ K}$) will be eventually destroyed in the harsh environment (e.g., the high-velocity shock and/or the surrounding warm/hot winds, $n \sim 10^{-3}\text{--}1 \text{ cm}^{-3}$ and $T \gtrsim 10^4 \text{ K}$). The cloud-crushing time (e.g., Klein et al. 1994) can be defined as $t_{\text{cc}} = \chi^{\frac{1}{2}} \frac{2r_{\text{cloud}}}{v_w}$, where $\chi = \frac{\rho_{\text{cloud}}}{\rho_{\text{wind}}}$ is the density contrast between the cloud and the wind, r_{cloud} is the cloud radius, and v_w is the wind velocity.

By adopting $\chi = 1000$ and $v_w = 200 \text{ km s}^{-1} = v_{w200}$ (see Section 3.4.1), we find that the crushing time of the high- z MCs is $t_{\text{cc}} \sim 0.9 v_{w200}^{-1} \text{ Myr}$ for the typical EHMC radius of $r_{\text{cloud}}=3 \text{ pc}$. The crushing time of the EHMCs is slightly small compared to the dynamical time of the gas flows (i.e., $t_{\text{dyn}} = \frac{l}{v_w} \gtrsim 1.3 v_{w200}^{-1} \text{ Myr}$, where the moving distance of gas flows is $l \gtrsim 260 \text{ pc}$ for the EHMCs). Note that changing $\chi = 1000$ to $\chi = 100$ will decrease the crushing time by a factor of ~ 3 . The smaller clouds (e.g., $r_{\text{cloud}} \ll 1 \text{ pc}$) thus could not survive long in the high-velocity wind.

For a more realistic case, however, EHMCs with parsec scales likely survive for a long period of time (e.g., a few Myr for several times of t_{cc}) in the gas-rich environment by considering the radiative cooling, condensation of gas from warm clouds, and some other effects (see, e.g., McCourt et al. 2015; Armillotta et al. 2017; Gronke & Oh 2018, 2020; Gronke et al. 2022; Banda-Barragán et al. 2019; Schneider et al. 2020; Sparre et al. 2020; Girichidis et al. 2021; Kanjilal et al. 2021; Farber & Gronke 2022).

As an interesting example, adopting the velocity gradient of $\sim 1 \text{ km s}^{-1} \text{ pc}^{-1}$ for EHMC G021.548–03.414 with the projection correction (Section 3.3), its dynamic time is estimated to be $t_{\text{dyn}} = t_{\text{acc}} = 2 \times \frac{\Delta \text{length}}{\Delta v} \sim 2.0 \text{ Myr}$, which is comparable to its crushing time of $t_{\text{cc}} \sim 2.2 v_{w200}^{-1} \text{ Myr}$ for its effective radius of 7.2 pc (see Table 1). The long tail of the cloud, together with the revealed velocity gradient, indicates that the molecular gas is ablated by the surrounding high-velocity wind. The molecular gas of the cloud is entrained in the multiphase flows, in which the molecular gas will be transformed to the neutral atomic and/or warm ionized gas moving toward the high- z regions. We suggest that the EHMC is crushed and will be destroyed in future several Myr. Thus, the lifetime of

the EHMC at $|z| \sim 450$ pc far from the Galactic plane is probably ~ 5 – 10 Myr, which is much longer than its crushing time.

Our CO observations reveal large reservoirs of cool gas surrounding the boundaries of the large-scale nuclear wind near the gaseous disk. That is, the abundant atomic gas is concentrated in the crater-wall structures that the dense EHMCS are embedded in (Sections 3.2 and 3.3). The EHMCS thus are not isolated objects situated in an empty space. The gas-rich environment with the local high density increases the survival ability of MCs in the crater walls.

For example, mass loading from the gaseous disk to the crater walls can flatten the density and temperature profiles on the boundary of the wind bubbles, creating multiphase flows in such regions. The multiphase gas-rich environment may cool fast to replenish the cold gas reservoir and then extend the lifetime of the high- z MCs. Additionally, the newly cooled gas from the surrounding high-velocity flows can carry momentum of the hot gas, leading to the observed entrainment scenario in the porous and mixed multiphase medium.

Nearly no EHMC is observed in the regions of $R_{GC} \lesssim 2.6$ kpc (Figure 2). There are two plausible reasons for the feature. One is that high- z clouds are indeed destroyed by the hot winds, in which the wind velocity in the nuclear wind bubble is higher than that near the boundary of the bubble. The molecular gas of the clouds may be rapidly transformed to the warm/hot ionized gas (e.g., $t_{cc} \lesssim 0.2$ Myr for the high-velocity wind with $v_w = 1000$ km s $^{-1}$ and $T \gtrsim 10^6$ K). The ionized gas moves fast toward the high- z regions, in which little cool gas can survive in the hot flows. On the other hand, our EHMC samples are from the CO emission toward the tangent points. The EHMC samples only occupy a small volume of the bubble in a certain LOS. It thus decreases the detection rate of possibly survived high- z MCs with an origin size of tens of parsecs in the hot wind bubble.

Finally, we emphasize that the cloud, and even the ISM, is inherently complex in its structure rather than the isolated and homogenous distribution in temperature, velocity, and density. The mean volume density of the EHMCS is ~ 20 H $_2$ cm $^{-3}$, much below the CO critical density of $3000/\tau_{12CO}$ H $_2$ cm $^{-3}$ (see, e.g., Scoville 2013; Shirley 2015). This probably shows that the EHMCS consist of clumpy and multiphase medium, in which the highly structured molecular gas with a low volume filling factor is mixed with more diffuse gas (e.g., Falgarone et al. 1991, 1992; Falgarone & Phillips 1996; Snow & McCall 2006; Hacar et al. 2016).

The original material in the MCs is heated into the multiphase gas (i.e., ionized/atomic/molecular) and entrained as it mixed with the warm/hot wind. Once the cloud material is entrained, it may quickly cool back down to the molecular phase in the enhanced gas+dust environment. In such a scenario, many effects (e.g., conduction and cooling, magnetic field and cosmic rays, and various instabilities) should be carefully taken into account for the interaction between the fractal MCs and the warm/hot wind. Detailed analysis of these effects is beyond the scope of this paper. More multi-wavelength observations and simulations will be very helpful to clarify these issues.

3.4.4. *Milky Way Nuclear Wind and the Gaseous Disk*

In the crater-wall regions (i.e., $|z| \sim 260$ – 670 pc and $R_{GC} \sim 3$ kpc), the total mass of the molecular gas is $\gtrsim 1 \times 10^6 M_\odot$. For the highest EHMC at $|z| \sim 620$ pc, its dynamical time is estimated to be $t_{\text{dyn}} = \frac{620 \text{ pc}}{v_{w200}} \lesssim 3.0 v_{w200}^{-1}$ Myr. The mass-loading rate from the inner gaseous disk of $R_{GC} \lesssim 3$ kpc to the high- z regions is thus $\gtrsim 0.3 v_{w200} M_\odot \text{ yr}^{-1}$.

If we take into account the disturbed MCs in the region close to the Galactic plane (e.g., $110 \text{ pc} \lesssim |z| \lesssim 260 \text{ pc}$), the true mass-loading rate may be increased by a factor of ~ 10 by assuming

a Gaussian distribution (e.g., the total mass is ~ 10 times of that in $|z| \gtrsim 260$ pc regions for the thick CO disk of $\sigma_z \sim 110\text{--}120$ pc; see [Su et al. 2021](#)). By considering the neutral atomic gas coexisting with the molecular gas, the mass-loading rate of the cool outflows may be slightly larger than the estimated value of $\sim 3v_{w200} M_\odot \text{ yr}^{-1}$. Although large uncertainty remains and more observations are needed, the rough estimate shows that the outflow rate at the order of $\sim 2 - 4 M_\odot \text{ yr}^{-1}$ is possible according to the large-scale enhanced CO emission at $R_{GC} \sim 3$ kpc.

The energy source of the Milky Way nuclear wind is still being debated, i.e., intermittent activities from Sgr A* for AGN-like model vs. integrated effects of the stellar feedback from the CMZ for the starburst model. The total kinetic energy of the cool-gas outflows can be estimated as $E_K = 0.5M_{\text{gas}}v_w^2 \gtrsim 4 \times 10^{54}v_{w200}^2$ erg for the total molecular gas mass of $\gtrsim 1 \times 10^7 M_\odot$ at $|z| \gtrsim 110$ pc (e.g., about ~ 10 times of that in $|z| \gtrsim 260$ pc regions). The required kinetic power to the pushed molecular gas is then $\sim 4 \times 10^{40}v_{w200}^3$ erg s^{-1} for the assumed dynamical time of $\sim 3.0v_{w200}^{-1}$ Myr. Whatever the exact origin of the Milky Way nuclear wind, our estimates show that the cool-gas outflows can be easily powered by the energetic processes near the GC (e.g., the total energy of $10^{56} - 10^{57}$ erg or the total power of $10^{42} - 10^{44}$ erg s^{-1} for the Fermi bubbles).

On the other hand, low-density gas can be easily accelerated in the hot wind environment. And the hot ionized gas is probably the dominant reservoir of energy of the Fermi bubbles (e.g., the inferred temperature of $\gtrsim 2 \times 10^6$ K, the low density of $\sim 10^{-3} \text{ cm}^{-3}$, and the typical velocity of $\sim 500 - 1000 \text{ km s}^{-1}$ for the hot gas; [Miller & Bregman 2016](#); [Bordoloi et al. 2017](#)). The warm and hot ionized gas of the nuclear wind plays an important role in driving the cool-gas outflows near the gaseous disk. Accordingly, the ablated gas from the high-structured MCs in the gaseous disk joins the moving flow, modifying the velocity, temperature, and density distribution of the multi-phase medium.

The thinner disk of the atomic and molecular gas within the region of $R_{GC} \lesssim 3$ kpc can be explained by the effect of the large-scale Milky Way nuclear wind. Assuming the hot wind velocity of $\sim 500 - 1000 \text{ km s}^{-1}$ and the mass-lose rate of $\sim 10 - 20 M_\odot \text{ yr}^{-1}$ near the Galactic inner gaseous disk, the disk will lose $\sim 6 \times 10^7 M_\odot$ in a period of $\sim 3\text{--}6$ Myr (e.g., from the CMZ to the $R_{GC} \sim 3$ kpc regions), which is about 30% of the molecular gas within the $R_{GC} \lesssim 3$ kpc region (e.g., the total molecular mass of $\sim 2 \times 10^8 M_\odot$, see [Heyer & Dame 2015](#); [Nakanishi & Sofue 2016](#)). Therefore, a bulk of the molecular gas can be removed from the gaseous disk within $R_{GC} \lesssim 3$ kpc, especially for the region of $|z| \gtrsim 50\text{--}100$ pc.

The total mass of the removed molecular gas in the inner disk is roughly comparable to the value of $\sim 7 \times 10^7 M_\odot$ for the whole 3-kpc arm (e.g., refer to H_2 masses per unit length of $\sim 4 \times 10^6 M_\odot \text{ kpc}^{-1}$ in [Dame & Thaddeus 2008](#)). We propose that the 3-kpc arm is probably related to the Milky Way nuclear wind. It is true that only a small fraction of molecular gas ($\gtrsim 1 \times 10^6 M_\odot$) is accelerated to the $|z| \gtrsim 260$ pc region, while the dominant molecular gas seems to be accumulated at the disk (e.g., the 3-kpc arm; see [Dame & Thaddeus 2008](#); [Reid et al. 2019](#); [Sofue & Kataoka 2021](#)). Both of the crater-walls traced by EHMCs and the 3-kpc arm are naturally located at the similar Galactocentric distance of $R_{GC} \sim 3$ kpc, where the high-velocity hot wind is almost stopped and/or is confined by the cold gas near the gaseous disk.

Due to angular momentum conservation, gas inflows generally accompany with gas outflows. The current star formation rate in the CMZ is $\lesssim 0.1 M_\odot \text{ yr}^{-1}$ (e.g., [Yusef-Zadeh et al. 2009](#); [Longmore et al. 2013](#)), which will exhaust the CMZ gas in a few $\times 10^8$ Myr without other gas sup-

ply. The continuous gas inflow from the inner disk may provide additional gas supply for the star formation in the CMZ (e.g., the inflow rate at the order of $\sim 1 - 4 M_{\odot} \text{ yr}^{-1}$; see [Armillotta et al. 2019](#); [Sormani & Barnes 2019](#); [Tress et al. 2020](#); [Hatchfield et al. 2021](#)).

The estimated mass outflow rate based on the CO data is roughly comparable to the gas inflow rate from the simulations at the same order of magnitude of $\sim 2 - 4 M_{\odot} \text{ yr}^{-1}$. Generally, the gas is transported from the inner gaseous disk at $R_{\text{GC}} \sim 3$ kpc to the CMZ by inflows, while the angular momentum of gas is taken away by outflows from the inner disk. The removed gas in the inner disk may fall back to the disk (e.g., the fountain models; [Shapiro & Field 1976](#); [Bregman 1980](#); [Houck & Bregman 1990](#); [Spitoni et al. 2008](#); [Melioli et al. 2009](#); [Marasco et al. 2015](#); [Fraternali 2017](#)) and/or may be accumulated in the 3-kpc arm and the high- z crater walls. In this regard, the total molecular gas mass in the CMZ should be roughly comparable to that in the 3-kpc arm.

Briefly, the existence of the outflows and the inflows is probably the common feature in the inner region of the Milky Way (or other barred spiral galaxies). The dynamical processes indicate that there is a delicate balance between gas outflows and inflows toward the inner region of the Milky Way. Highly variable inflow rate from a recent epoch may lead to the episodic accretion onto the CMZ and intermittent activity from Sgr A* (see, e.g., recent observations in [Ponti et al. 2019, 2021](#)). The following enhanced outflows will then terminate star formation near the GC and/or restrain nuclear activity due to decreasing the gas supply.

Finally, Figure 7 shows a schematic view of the observation results, i.e., the large-scale HI voids related to the Fermi bubbles/X-ray bubbles in the inner Galaxy, the CO crater walls surrounding the edges of the HI voids above and below the Galactic plane, the thinner gaseous disk within $R_{\text{GC}} \lesssim 3$ kpc, the expanding 3-kpc arm at the base of the enhanced EHMCs, and the entrained MCs with cometary structures pointing away from the Galactic plane.

4. SUMMARY

Based on the MWISP CO data and the improved criteria of the DBSCAN algorithm, we construct high- z MC samples near the tangent points, in which the distances of the MCs are well determined. In the region of $l = 12^{\circ} - 26^{\circ}$ and $|b| \lesssim 5^{\circ}1$, a total of 321 high- z MCs (i.e., MCs at $|z| \gtrsim 110$ pc) are identified, of which 47 MCs lie in the extreme high- z regions (i.e., EHMCs at $|z| \gtrsim 260$ pc). Besides the weak CO emission and small sizes, these high- z MCs also display some unusual properties:

1. The high- z MCs in the $R_{\text{GC}} \lesssim 3$ kpc region are significantly less than that of the outer region, which is consistent with the deficient atomic gas and molecular gas in the inner Galactic disk of $R_{\text{GC}} \lesssim 3$ kpc.

2. The EHMCs (i.e., IDs 05–31 in Table 1) are mainly concentrated in narrow regions of $[l \sim 19^{\circ}1$ to $20^{\circ}5, b \sim 2^{\circ}0$ to $5^{\circ}1]$ and $[l \sim 20^{\circ}5$ to $22^{\circ}1, b \sim -2^{\circ}0$ to $-5^{\circ}1]$. Some EHMCs are even located at $|z| \gtrsim 600$ pc far above and below the Galactic plane. The EHMC concentrations, together with other high- z MCs at $l \lesssim 18^{\circ}$, constitute molecular crater-walls with a measured thickness of ~ 220 pc. The molecular crater wall structures lie along the edges of the HI voids (Figure 1) that are associated with the Milky Way nuclear wind (e.g., [Lockman & McClure-Griffiths 2016](#); [Sofue & Kataoka 2021](#)).

3. Some large high- z MCs, which lie in the crater walls, display intriguing elongated head-to-tail structures pointing away from the Galactic disk, favoring the scenario of the entrained molecular gas moving with the multiphase outflows. Especially, the ~ 20 pc long tail of the EHMC G021.548–03.414 (Figure 3) is physically associated with a filamentary structure of the IR dust emission, which is exactly located in the enhanced HI ridge. The observed velocity gradient of the

EHMC (Figure 4), together with its cometary head toward the Galactic plane, shows that the cold molecular gas is indeed entrained by the multiphase outflows from the Galactic plane to the high- z regions.

Based on the above results, we suggest that the powerful nuclear wind of the Milky Way has a profound impact on the large-scale distribution of the gaseous disk (Figure 7). The HI voids above and below the Galactic plane, the CO crater walls at the edges of the HI voids, and the expanding 3-kpc arms at the base of the molecular crater walls are probably the natural result of the intermittent nuclear activity of the Milky Way in the recent 3–6 Myr.

The cometary MCs lying in the crater walls show that the nuclear wind removes gas from the inner Galaxy to the high- z regions. The cold gas in the crater-wall structures at $R_{GC} \sim 3$ kpc plays a crucial role confining the Milky Way nuclear wind. The cool outflows may be an important mass reservoir for supplying halo material that has been pushed up from the interface between the nuclear wind and the gaseous disk within $R_{GC} \lesssim 3$ kpc. In this scenario, some interesting estimates can be summarized as follows:

1. The gas-rich environment increases the survival ability of the EHMCs in the crater walls with the local high density of $\sim 1\text{--}10\text{ cm}^{-3}$ for HI clouds and $\sim 10^2\text{--}10^3\text{ cm}^{-3}$ for CO clouds. The estimated lifetime of EHMCs is several Myr for clouds on the parsec scales, which is comparable to the dynamical time of the cool gas flows according to the observed velocity gradient of the CO gas (i.e., $\sim 0.5\text{--}1\text{ km s}^{-1}\text{pc}^{-1}$ after the projection correction with a small inclination angle of $i \sim 20^\circ\text{--}10^\circ$). Basically, the observed EHMCs in the walls will be destroyed in future several Myr. The MCs thus cannot move too far away from the Galactic plane (e.g., $|z| \gtrsim 1$ kpc) before the molecular gas becomes the neutral atomic gas and/or ionized gas.

2. The velocity of the cool outflows is estimated to be $\sim 140\text{--}330\text{ km s}^{-1}$ assuming that the gas is launched from the boundary of the thin CO disk (i.e., from $|z| = 3 \times \sigma_z \sim 110\text{--}120$ pc; Su et al. 2021). The hypothesis is supported by the observed cometary high- z MCs pointing away from the Galactic plane at locations of $|z| \sim 110\text{--}130$ pc (top panels of Figure 5) and the large-scale velocity gradient of the coherent EHMCs at $|z| \sim 400\text{--}450$ pc far from the plane (see Figure 6).

3. The molecular gas in the EHMC concentrations of $\sim 2 \times 220\text{ pc} \times 410\text{ pc}$ has a total mass of $\gtrsim 1 \times 10^4 M_\odot$ (Figure 2). If the extreme high- z MCs are more broadly distributed in the whole regions of $R_{GC} \sim 3$ kpc, $|z| \sim 260\text{--}670$ pc, and the wall's thickness of ~ 220 pc, the total molecular mass is estimated to be $\gtrsim 1 \times 10^6 M_\odot$, which is comparable to the total HI mass in the Fermi bubbles (Di Teodoro et al. 2018; Lockman et al. 2020).

4. Assuming a Gaussian distribution for the thick CO disk (i.e., $\sigma_z = 120$ pc and the thickness $\text{FWHM} = 2.355\sigma_z$ in Su et al. 2021), a significant amount of molecular gas (e.g., the order of $10^7 M_\odot$) may accumulate at the low latitudes of the gaseous disk of $|z| \sim 110\text{--}260$ pc. The mass-loading rate of the cool outflows at $R_{GC} \sim 3$ kpc (i.e., outflows to the crater-wall structures) is roughly comparable to the mass inflow rate (i.e., inflows to the CMZ) at the same order of $\sim 2\text{--}4 M_\odot\text{ yr}^{-1}$.

5. The thinner gas disk within $R_{GC} \lesssim 3$ kpc may be the joint result of (1) inflows from the inner gaseous disk to the CMZ and (2) outflows from the gaseous disk to the 3-kpc arm and the high- z region. The 3-kpc arm at the base of the EHMC concentration, together with the thinner gaseous disk within $R_{GC} \lesssim 3$ kpc, can be naturally explained by the interaction between the Milky Way nuclear wind and the Galactic gaseous disk.

Considering the large uncertainties in the discussions, the above estimates should be used with caution. Nevertheless, we think that the results are useful for further studies. For example, the multiwavelength observations (e.g., radio continuum, millimeter and submillimeter molecular line emission, optical/near-IR emission lines, and UV absorption) are advocated to investigate the physical properties of the cometary high- z MCs. The large-scale surveys with high sensitivity and high resolution, together with the improved simulations, are also very helpful to reveal the nature of the Galactic nuclear winds/outflows.

ACKNOWLEDGMENTS

This research made use of the data from the Milky Way Imaging Scroll Painting (MWISP) project, which is a multiline survey in $^{12}\text{CO}/^{13}\text{CO}/\text{C}^{18}\text{O}$ along the northern Galactic plane with the PMO 13.7m telescope. We are grateful to all the members of the MWISP working group, particularly the staff members at the PMO 13.7m telescope, for their long-term support. MWISP was sponsored by the National Key R&D Program of China with grant 2017YFA0402700 and the CAS Key Research Program of Frontier Sciences with grant QYZDJ-SSW-SLH047. We acknowledge support from the National Natural Science Foundation of China through grants 12173090 and 12041305. X.C. acknowledges support by the CAS International Cooperation Program (grant No. 114332KYSB20190009). We also thank the anonymous referee for many useful and constructive comments that largely improved the quality of the paper.

The work makes use of publicly released data from the HI4PI survey, which combines the EBHIS in the Northern hemisphere with the GASS in the Southern Hemisphere. The Parkes Radio Telescope is part of the Australia Telescope National Facility, which is funded by the Australian Government for operation as a National Facility managed by CSIRO. The EBHIS data are based on observations performed with the 100 m telescope of the MPIfR at Effelsberg. EBHIS was funded by the Deutsche Forschungsgemeinschaft (DFG) under the grants KE757/7-1 to 7-3. This publication makes use of data products from the Wide-field Infrared Survey Explorer, which is a joint project of the University of California, Los Angeles, and the Jet Propulsion Laboratory/California Institute of Technology, funded by the National Aeronautics and Space Administration.

Facility: PMO 13.7m

Software: GILDAS/CLASS (Pety 2005)

REFERENCES

- Ackermann, M., Albert, A., Atwood, W. B., et al. 2014, *ApJ*, 793, 64, doi: [10.1088/0004-637X/793/1/64](https://doi.org/10.1088/0004-637X/793/1/64)
- Armillotta, L., Fraternali, F., Werk, J. K., Prochaska, J. X., & Marinacci, F. 2017, *MNRAS*, 470, 114, doi: [10.1093/mnras/stx1239](https://doi.org/10.1093/mnras/stx1239)
- Armillotta, L., Krumholz, M. R., Di Teodoro, E. M., & McClure-Griffiths, N. M. 2019, *MNRAS*, 490, 4401, doi: [10.1093/mnras/stz2880](https://doi.org/10.1093/mnras/stz2880)
- Ashley, T., Fox, A. J., Jenkins, E. B., et al. 2020, *ApJ*, 898, 128, doi: [10.3847/1538-4357/ab9ff8](https://doi.org/10.3847/1538-4357/ab9ff8)
- Banda-Barragán, W. E., Brüggen, M., Heesen, V., et al. 2021, *MNRAS*, 506, 5658, doi: [10.1093/mnras/stab1884](https://doi.org/10.1093/mnras/stab1884)
- Banda-Barragán, W. E., Zertuche, F. J., Federrath, C., et al. 2019, *MNRAS*, 486, 4526, doi: [10.1093/mnras/stz1040](https://doi.org/10.1093/mnras/stz1040)
- Bland-Hawthorn, J., & Cohen, M. 2003, *ApJ*, 582, 246, doi: [10.1086/344573](https://doi.org/10.1086/344573)

- Bolatto, A. D., Wolfire, M., & Leroy, A. K. 2013a, *ARA&A*, 51, 207, doi: [10.1146/annurev-astro-082812-140944](https://doi.org/10.1146/annurev-astro-082812-140944)
- Bolatto, A. D., Warren, S. R., Leroy, A. K., et al. 2013b, *Nature*, 499, 450, doi: [10.1038/nature12351](https://doi.org/10.1038/nature12351)
- Bordoloi, R., Fox, A. J., Lockman, F. J., et al. 2017, *ApJ*, 834, 191, doi: [10.3847/1538-4357/834/2/191](https://doi.org/10.3847/1538-4357/834/2/191)
- Bregman, J. N. 1980, *ApJ*, 236, 577, doi: [10.1086/157776](https://doi.org/10.1086/157776)
- Burton, W. B. 1976, *ARA&A*, 14, 275, doi: [10.1146/annurev.aa.14.090176.001423](https://doi.org/10.1146/annurev.aa.14.090176.001423)
- Burton, W. B., Elmegreen, B. G., Genzel, R., Pfenniger, D., & Bartholdi, P. 1992, in *Saas-Fee Advanced Course 21: The Galactic Interstellar Medium* (Berlin: Springer)
- Burton, W. B., & Gordon, M. A. 1977, in *Astrophysics and Space Science Library*, Vol. 70, *Topics in Interstellar Matter*, ed. H. van Woerden, 165, doi: [10.1007/978-94-010-1254-6_18](https://doi.org/10.1007/978-94-010-1254-6_18)
- Burton, W. B., Gordon, M. A., Bania, T. M., & Lockman, F. J. 1975, *ApJ*, 202, 30, doi: [10.1086/153950](https://doi.org/10.1086/153950)
- Carretti, E., Crocker, R. M., Staveley-Smith, L., et al. 2013, *Nature*, 493, 66, doi: [10.1038/nature11734](https://doi.org/10.1038/nature11734)
- Cashman, F. H., Fox, A. J., Savage, B. D., et al. 2021, *ApJL*, 923, L11, doi: [10.3847/2041-8213/ac3cbc](https://doi.org/10.3847/2041-8213/ac3cbc)
- Cecil, G., Wagner, A. Y., Bland-Hawthorn, J., Bicknell, G. V., & Mukherjee, D. 2021, *ApJ*, 922, 254, doi: [10.3847/1538-4357/ac224f](https://doi.org/10.3847/1538-4357/ac224f)
- Combes, F. 1991, *ARA&A*, 29, 195, doi: [10.1146/annurev.aa.29.090191.001211](https://doi.org/10.1146/annurev.aa.29.090191.001211)
- Crocker, R. M., Bicknell, G. V., Taylor, A. M., & Carretti, E. 2015, *ApJ*, 808, 107, doi: [10.1088/0004-637X/808/2/107](https://doi.org/10.1088/0004-637X/808/2/107)
- Dame, T. M., Hartmann, D., & Thaddeus, P. 2001, *ApJ*, 547, 792, doi: [10.1086/318388](https://doi.org/10.1086/318388)
- Dame, T. M., & Thaddeus, P. 2008, *ApJL*, 683, L143, doi: [10.1086/591669](https://doi.org/10.1086/591669)
- Di Teodoro, E. M., McClure-Griffiths, N. M., Lockman, F. J., & Armillotta, L. 2020, *Nature*, 584, 364, doi: [10.1038/s41586-020-2595-z](https://doi.org/10.1038/s41586-020-2595-z)
- Di Teodoro, E. M., McClure-Griffiths, N. M., Lockman, F. J., et al. 2018, *ApJ*, 855, 33, doi: [10.3847/1538-4357/aaad6a](https://doi.org/10.3847/1538-4357/aaad6a)
- Dickey, J. M., & Lockman, F. J. 1990, *ARA&A*, 28, 215, doi: [10.1146/annurev.aa.28.090190.001243](https://doi.org/10.1146/annurev.aa.28.090190.001243)
- Falgarone, E., & Phillips, T. G. 1996, *ApJ*, 472, 191, doi: [10.1086/178054](https://doi.org/10.1086/178054)
- Falgarone, E., Phillips, T. G., & Walker, C. K. 1991, *ApJ*, 378, 186, doi: [10.1086/170419](https://doi.org/10.1086/170419)
- Falgarone, E., Puget, J. L., & Perault, M. 1992, *A&A*, 257, 715
- Fang, X.-E., Guo, F., & Yuan, Y.-F. 2020, *ApJ*, 894, 1, doi: [10.3847/1538-4357/ab846c](https://doi.org/10.3847/1538-4357/ab846c)
- Farber, R. J., & Gronke, M. 2022, *MNRAS*, 510, 551, doi: [10.1093/mnras/stab3412](https://doi.org/10.1093/mnras/stab3412)
- Fielding, D. B., & Bryan, G. L. 2022, *ApJ*, 924, 82, doi: [10.3847/1538-4357/ac2f41](https://doi.org/10.3847/1538-4357/ac2f41)
- Ford, H. A., Lockman, F. J., & McClure-Griffiths, N. M. 2010, *ApJ*, 722, 367, doi: [10.1088/0004-637X/722/1/367](https://doi.org/10.1088/0004-637X/722/1/367)
- Ford, H. A., McClure-Griffiths, N. M., Lockman, F. J., et al. 2008, *ApJ*, 688, 290, doi: [10.1086/592188](https://doi.org/10.1086/592188)
- Fox, A. J., Bordoloi, R., Savage, B. D., et al. 2015, *ApJL*, 799, L7, doi: [10.1088/2041-8205/799/1/L7](https://doi.org/10.1088/2041-8205/799/1/L7)
- Fraternali, F. 2017, in *Astrophysics and Space Science Library*, Vol. 430, *Gas Accretion onto Galaxies*, ed. A. Fox & R. Davé, 323, doi: [10.1007/978-3-319-52512-9_14](https://doi.org/10.1007/978-3-319-52512-9_14)
- Fraternali, F., & Binney, J. J. 2008, *MNRAS*, 386, 935, doi: [10.1111/j.1365-2966.2008.13071.x](https://doi.org/10.1111/j.1365-2966.2008.13071.x)
- Girichidis, P., Naab, T., Walch, S., & Berlok, T. 2021, *MNRAS*, 505, 1083, doi: [10.1093/mnras/stab1203](https://doi.org/10.1093/mnras/stab1203)
- Gronke, M., & Oh, S. P. 2018, *MNRAS*, 480, L111, doi: [10.1093/mnrasl/sly131](https://doi.org/10.1093/mnrasl/sly131)
- . 2020, *MNRAS*, 492, 1970, doi: [10.1093/mnras/stz3332](https://doi.org/10.1093/mnras/stz3332)
- Gronke, M., Oh, S. P., Ji, S., & Norman, C. 2022, *MNRAS*, 511, 859, doi: [10.1093/mnras/stab3351](https://doi.org/10.1093/mnras/stab3351)
- Hacar, A., Alves, J., Burkert, A., & Goldsmith, P. 2016, *A&A*, 591, A104, doi: [10.1051/0004-6361/201527319](https://doi.org/10.1051/0004-6361/201527319)
- Hatchfield, H. P., Sormani, M. C., Tress, R. G., et al. 2021, *ApJ*, 922, 79, doi: [10.3847/1538-4357/ac1e89](https://doi.org/10.3847/1538-4357/ac1e89)
- Heyer, M., & Dame, T. M. 2015, *ARA&A*, 53, 583, doi: [10.1146/annurev-astro-082214-122324](https://doi.org/10.1146/annurev-astro-082214-122324)
- Heywood, I., Camilo, F., Cotton, W. D., et al. 2019, *Nature*, 573, 235, doi: [10.1038/s41586-019-1532-5](https://doi.org/10.1038/s41586-019-1532-5)

- HI4PI Collaboration, Ben Bekhti, N., Flöer, L., et al. 2016, *A&A*, 594, A116, doi: [10.1051/0004-6361/201629178](https://doi.org/10.1051/0004-6361/201629178)
- Holt, J., Tadhunter, C. N., & Morganti, R. 2008, *MNRAS*, 387, 639, doi: [10.1111/j.1365-2966.2008.13089.x](https://doi.org/10.1111/j.1365-2966.2008.13089.x)
- Houck, J. C., & Bregman, J. N. 1990, *ApJ*, 352, 506, doi: [10.1086/168554](https://doi.org/10.1086/168554)
- Hsieh, P.-Y., Ho, P. T. P., Hwang, C.-Y., et al. 2016, *ApJ*, 831, 72, doi: [10.3847/0004-637X/831/1/72](https://doi.org/10.3847/0004-637X/831/1/72)
- Kalberla, P. M. W., & Kerp, J. 2009, *ARA&A*, 47, 27, doi: [10.1146/annurev-astro-082708-101823](https://doi.org/10.1146/annurev-astro-082708-101823)
- Kanjilal, V., Dutta, A., & Sharma, P. 2021, *MNRAS*, 501, 1143, doi: [10.1093/mnras/staa3610](https://doi.org/10.1093/mnras/staa3610)
- Karim, T., Fox, A. J., Jenkins, E. B., et al. 2018, *ApJ*, 860, 98, doi: [10.3847/1538-4357/aac167](https://doi.org/10.3847/1538-4357/aac167)
- Kataoka, J., Tahara, M., Totani, T., et al. 2013, *ApJ*, 779, 57, doi: [10.1088/0004-637X/779/1/57](https://doi.org/10.1088/0004-637X/779/1/57)
- Keeney, B. A., Danforth, C. W., Stocke, J. T., et al. 2006, *ApJ*, 646, 951, doi: [10.1086/505128](https://doi.org/10.1086/505128)
- Klein, R. I., McKee, C. F., & Colella, P. 1994, *ApJ*, 420, 213, doi: [10.1086/173554](https://doi.org/10.1086/173554)
- Krieger, N., Bolatto, A. D., Walter, F., et al. 2019, *ApJ*, 881, 43, doi: [10.3847/1538-4357/ab2d9c](https://doi.org/10.3847/1538-4357/ab2d9c)
- Krieger, N., Walter, F., Bolatto, A. D., et al. 2021, *ApJL*, 915, L3, doi: [10.3847/2041-8213/ac01e9](https://doi.org/10.3847/2041-8213/ac01e9)
- Krishnarao, D., Benjamin, R. A., & Haffner, L. M. 2020, *ApJL*, 899, L11, doi: [10.3847/2041-8213/aba8f0](https://doi.org/10.3847/2041-8213/aba8f0)
- Leroy, A. K., Walter, F., Martini, P., et al. 2015, *ApJ*, 814, 83, doi: [10.1088/0004-637X/814/2/83](https://doi.org/10.1088/0004-637X/814/2/83)
- Lockman, F. J. 1984, *ApJ*, 283, 90, doi: [10.1086/162277](https://doi.org/10.1086/162277)
- Lockman, F. J., Di Teodoro, E. M., & McClure-Griffiths, N. M. 2020, *ApJ*, 888, 51, doi: [10.3847/1538-4357/ab55d8](https://doi.org/10.3847/1538-4357/ab55d8)
- Lockman, F. J., & McClure-Griffiths, N. M. 2016, *ApJ*, 826, 215, doi: [10.3847/0004-637X/826/2/215](https://doi.org/10.3847/0004-637X/826/2/215)
- Longmore, S. N., Bally, J., Testi, L., et al. 2013, *MNRAS*, 429, 987, doi: [10.1093/mnras/sts376](https://doi.org/10.1093/mnras/sts376)
- Malhotra, S. 1994, *ApJ*, 433, 687, doi: [10.1086/174677](https://doi.org/10.1086/174677)
- Marasco, A., Debattista, V. P., Fraternali, F., et al. 2015, *MNRAS*, 451, 4223, doi: [10.1093/mnras/stv1240](https://doi.org/10.1093/mnras/stv1240)
- McClure-Griffiths, N. M., Green, J. A., Hill, A. S., et al. 2013, *ApJL*, 770, L4, doi: [10.1088/2041-8205/770/1/L4](https://doi.org/10.1088/2041-8205/770/1/L4)
- McClure-Griffiths, N. M., Pisano, D. J., Calabretta, M. R., et al. 2009, *ApJS*, 181, 398, doi: [10.1088/0067-0049/181/2/398](https://doi.org/10.1088/0067-0049/181/2/398)
- McCourt, M., O’Leary, R. M., Madigan, A.-M., & Quataert, E. 2015, *MNRAS*, 449, 2, doi: [10.1093/mnras/stv355](https://doi.org/10.1093/mnras/stv355)
- Meier, D. S., Walter, F., Bolatto, A. D., et al. 2015, *ApJ*, 801, 63, doi: [10.1088/0004-637X/801/1/63](https://doi.org/10.1088/0004-637X/801/1/63)
- Melioli, C., Brighenti, F., D’Ercole, A., & de Gouveia Dal Pino, E. M. 2009, *MNRAS*, 399, 1089, doi: [10.1111/j.1365-2966.2009.14725.x](https://doi.org/10.1111/j.1365-2966.2009.14725.x)
- Miller, M. J., & Bregman, J. N. 2016, *ApJ*, 829, 9, doi: [10.3847/0004-637X/829/1/9](https://doi.org/10.3847/0004-637X/829/1/9)
- Mondal, S., Keshet, U., Sarkar, K. C., & Gurwich, I. 2021, arXiv e-prints, arXiv:2109.03834, <https://arxiv.org/abs/2109.03834>
- Morganti, R., Oosterloo, T., Murthy, S., & Tadhunter, C. 2021, *Astronomische Nachrichten*, 342, 1135, doi: [10.1002/asna.20210037](https://doi.org/10.1002/asna.20210037)
- Nakanishi, H., & Sofue, Y. 2016, *PASJ*, 68, 5, doi: [10.1093/pasj/psv108](https://doi.org/10.1093/pasj/psv108)
- Pety, J. 2005, in *SF2A-2005: Semaine de l’Astrophysique Francaise*, ed. F. Casoli, T. Contini, J. M. Hameury, & L. Pagani, (Les Ulis: EDP), 721
- Pidopryhora, Y., Lockman, F. J., & Shields, J. C. 2007, *ApJ*, 656, 928, doi: [10.1086/510521](https://doi.org/10.1086/510521)
- Pillepich, A., Nelson, D., Truong, N., et al. 2021, *MNRAS*, 508, 4667, doi: [10.1093/mnras/stab2779](https://doi.org/10.1093/mnras/stab2779)
- Ponti, G., Morris, M. R., Churazov, E., Heywood, I., & Fender, R. P. 2021, *A&A*, 646, A66, doi: [10.1051/0004-6361/202039636](https://doi.org/10.1051/0004-6361/202039636)
- Ponti, G., Hofmann, F., Churazov, E., et al. 2019, *Nature*, 567, 347, doi: [10.1038/s41586-019-1009-6](https://doi.org/10.1038/s41586-019-1009-6)
- Predehl, P., Sunyaev, R. A., Becker, W., et al. 2020, *Nature*, 588, 227, doi: [10.1038/s41586-020-2979-0](https://doi.org/10.1038/s41586-020-2979-0)
- Reid, M. J., Menten, K. M., Brunthaler, A., et al. 2019, *ApJ*, 885, 131, doi: [10.3847/1538-4357/ab4a11](https://doi.org/10.3847/1538-4357/ab4a11)
- Richings, A. J., & Faucher-Giguère, C.-A. 2018, *MNRAS*, 474, 3673, doi: [10.1093/mnras/stx3014](https://doi.org/10.1093/mnras/stx3014)

- Sarkar, K. C., Nath, B. B., & Sharma, P. 2015, *MNRAS*, 453, 3827, doi: [10.1093/mnras/stv1806](https://doi.org/10.1093/mnras/stv1806)
- Savage, B. D., Kim, T.-S., Fox, A. J., et al. 2017, *ApJS*, 232, 25, doi: [10.3847/1538-4365/aa8f4c](https://doi.org/10.3847/1538-4365/aa8f4c)
- Schneider, E. E., Ostriker, E. C., Robertson, B. E., & Thompson, T. A. 2020, *ApJ*, 895, 43, doi: [10.3847/1538-4357/ab8ae8](https://doi.org/10.3847/1538-4357/ab8ae8)
- Scoville, N. Z. 2013, Evolution of star formation and gas, ed. J. Falcón-Barroso & J. H. Knapen, 491
- Shapiro, P. R., & Field, G. B. 1976, *ApJ*, 205, 762, doi: [10.1086/154332](https://doi.org/10.1086/154332)
- Shirley, Y. L. 2015, *PASP*, 127, 299, doi: [10.1086/680342](https://doi.org/10.1086/680342)
- Snow, T. P., & McCall, B. J. 2006, *ARA&A*, 44, 367, doi: [10.1146/annurev.astro.43.072103.150624](https://doi.org/10.1146/annurev.astro.43.072103.150624)
- Sofue, Y. 2000, *ApJ*, 540, 224, doi: [10.1086/309297](https://doi.org/10.1086/309297)
- . 2017, *PASJ*, 69, L8, doi: [10.1093/pasj/psx067](https://doi.org/10.1093/pasj/psx067)
- Sofue, Y., & Handa, T. 1984, *Nature*, 310, 568, doi: [10.1038/310568a0](https://doi.org/10.1038/310568a0)
- Sofue, Y., & Kataoka, J. 2021, *MNRAS*, 506, 2170, doi: [10.1093/mnras/stab1857](https://doi.org/10.1093/mnras/stab1857)
- Sormani, M. C., & Barnes, A. T. 2019, *MNRAS*, 484, 1213, doi: [10.1093/mnras/stz046](https://doi.org/10.1093/mnras/stz046)
- Sparre, M., Pfrommer, C., & Ehlert, K. 2020, *MNRAS*, 499, 4261, doi: [10.1093/mnras/staa3177](https://doi.org/10.1093/mnras/staa3177)
- Spitoni, E., Recchi, S., & Matteucci, F. 2008, *A&A*, 484, 743, doi: [10.1051/0004-6361:200809403](https://doi.org/10.1051/0004-6361:200809403)
- Su, M., Slatyer, T. R., & Finkbeiner, D. P. 2010, *ApJ*, 724, 1044, doi: [10.1088/0004-637X/724/2/1044](https://doi.org/10.1088/0004-637X/724/2/1044)
- Su, Y., Zhou, X., Yang, J., et al. 2018, *ApJ*, 863, 103, doi: [10.3847/1538-4357/aad04e](https://doi.org/10.3847/1538-4357/aad04e)
- Su, Y., Yang, J., Zhang, S., et al. 2019, *ApJS*, 240, 9, doi: [10.3847/1538-4365/aaf1c8](https://doi.org/10.3847/1538-4365/aaf1c8)
- Su, Y., Yang, J., Yan, Q.-Z., et al. 2021, *ApJ*, 910, 131, doi: [10.3847/1538-4357/abe5ab](https://doi.org/10.3847/1538-4357/abe5ab)
- Tanner, R., & Weaver, K. A. 2022, *AJ*, 163, 134, doi: [10.3847/1538-3881/ac4d23](https://doi.org/10.3847/1538-3881/ac4d23)
- Tress, R. G., Sormani, M. C., Glover, S. C. O., et al. 2020, *MNRAS*, 499, 4455, doi: [10.1093/mnras/staa3120](https://doi.org/10.1093/mnras/staa3120)
- Veilleux, S., Cecil, G., & Bland-Hawthorn, J. 2005, *ARA&A*, 43, 769, doi: [10.1146/annurev.astro.43.072103.150610](https://doi.org/10.1146/annurev.astro.43.072103.150610)
- Veilleux, S., Maiolino, R., Bolatto, A. D., & Aalto, S. 2020, *A&A Rv*, 28, 2, doi: [10.1007/s00159-019-0121-9](https://doi.org/10.1007/s00159-019-0121-9)
- Walter, F., Bolatto, A. D., Leroy, A. K., et al. 2017, *ApJ*, 835, 265, doi: [10.3847/1538-4357/835/2/265](https://doi.org/10.3847/1538-4357/835/2/265)
- Wright, E. L., Eisenhardt, P. R. M., Mainzer, A. K., et al. 2010, *AJ*, 140, 1868, doi: [10.1088/0004-6256/140/6/1868](https://doi.org/10.1088/0004-6256/140/6/1868)
- Yan, Q.-Z., Yang, J., Su, Y., Sun, Y., & Wang, C. 2020, *ApJ*, 898, 80, doi: [10.3847/1538-4357/ab9f9c](https://doi.org/10.3847/1538-4357/ab9f9c)
- Yang, H. Y. K., Ruszkowski, M., & Zweibel, E. G. 2022, *Nature Astronomy*, doi: [10.1038/s41550-022-01618-x](https://doi.org/10.1038/s41550-022-01618-x)
- Yoshida, M., Kawabata, K. S., Ohya, Y., Itoh, R., & Hattori, T. 2019, *PASJ*, 71, 87, doi: [10.1093/pasj/psz069](https://doi.org/10.1093/pasj/psz069)
- Yusef-Zadeh, F., Hewitt, J. W., Arendt, R. G., et al. 2009, *ApJ*, 702, 178, doi: [10.1088/0004-637X/702/1/178](https://doi.org/10.1088/0004-637X/702/1/178)
- Zech, W. F., Lehner, N., Howk, J. C., Dixon, W. V. D., & Brown, T. M. 2008, *ApJ*, 679, 460, doi: [10.1086/587135](https://doi.org/10.1086/587135)
- Zhang, R., & Guo, F. 2020, *ApJ*, 894, 117, doi: [10.3847/1538-4357/ab8bd0](https://doi.org/10.3847/1538-4357/ab8bd0)

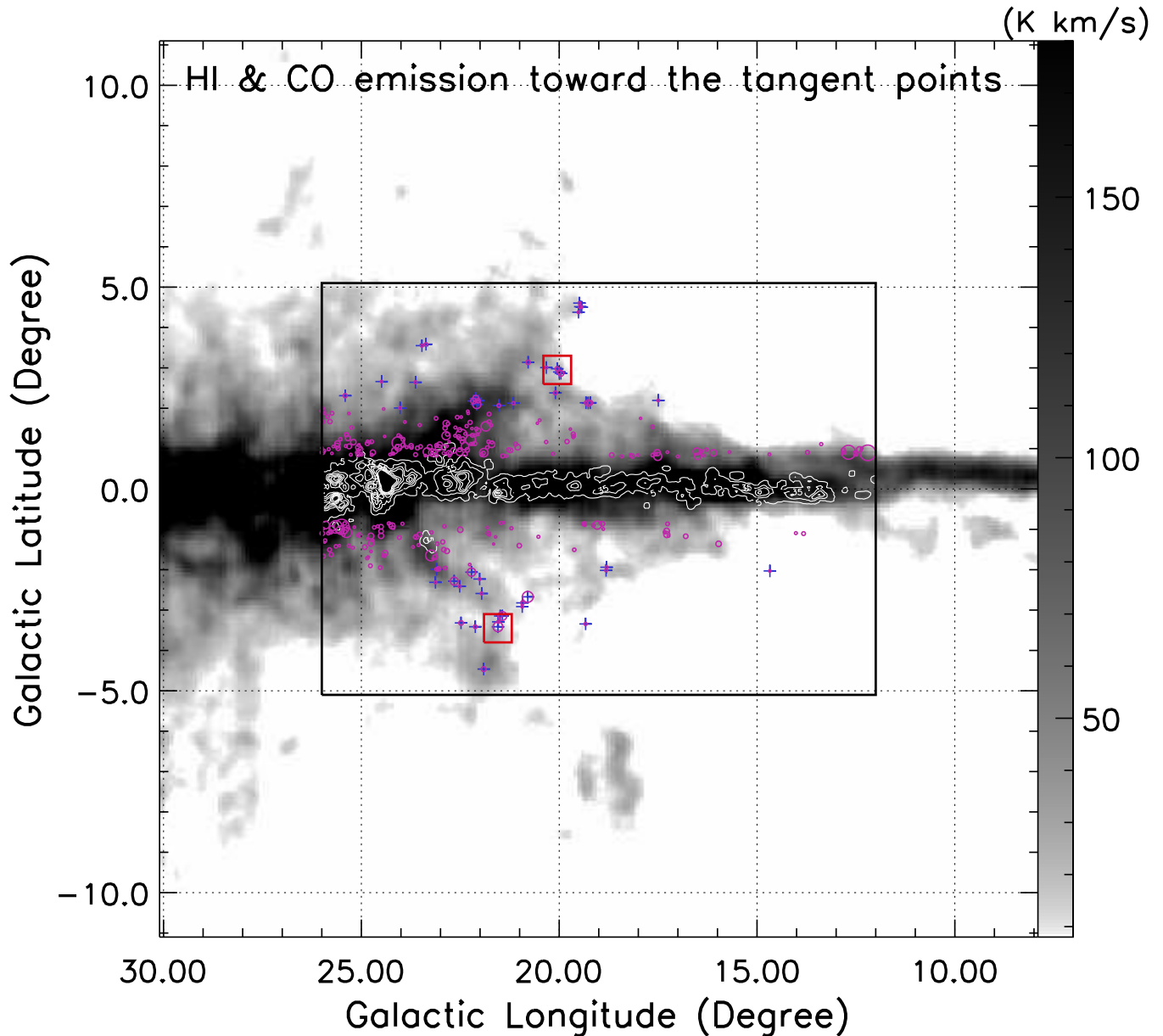


Figure 1. HI (gray) and CO (white contours) emission toward the tangent points. The atomic and molecular layers are clearly thin for regions of $l \lesssim 22^\circ$. The purple circles are 321 high- z MCs ($|z| \gtrsim 110$ pc) identified from the MWISP data in the region of $l = 12^\circ$ – 26° and $|b| \lesssim 5.1$ (the black rectangle). Note that the circle's size is not the true angular size of the MCs, but it is proportional to the effective radius of the clouds (i.e., $d \times \sqrt{(\theta_{\text{MC}}^2 - \theta_{\text{beam}}^2)}/\pi$, where θ_{MC} and θ_{beam} , in units of arcmin, are the angular size of the CO emission and the beam size, respectively). The blue plus signs indicate the positions of the 47 identified EHMCS (see Section 3.3 and Table 1). The red boxes indicate two zoom-in regions shown in Figure 3.

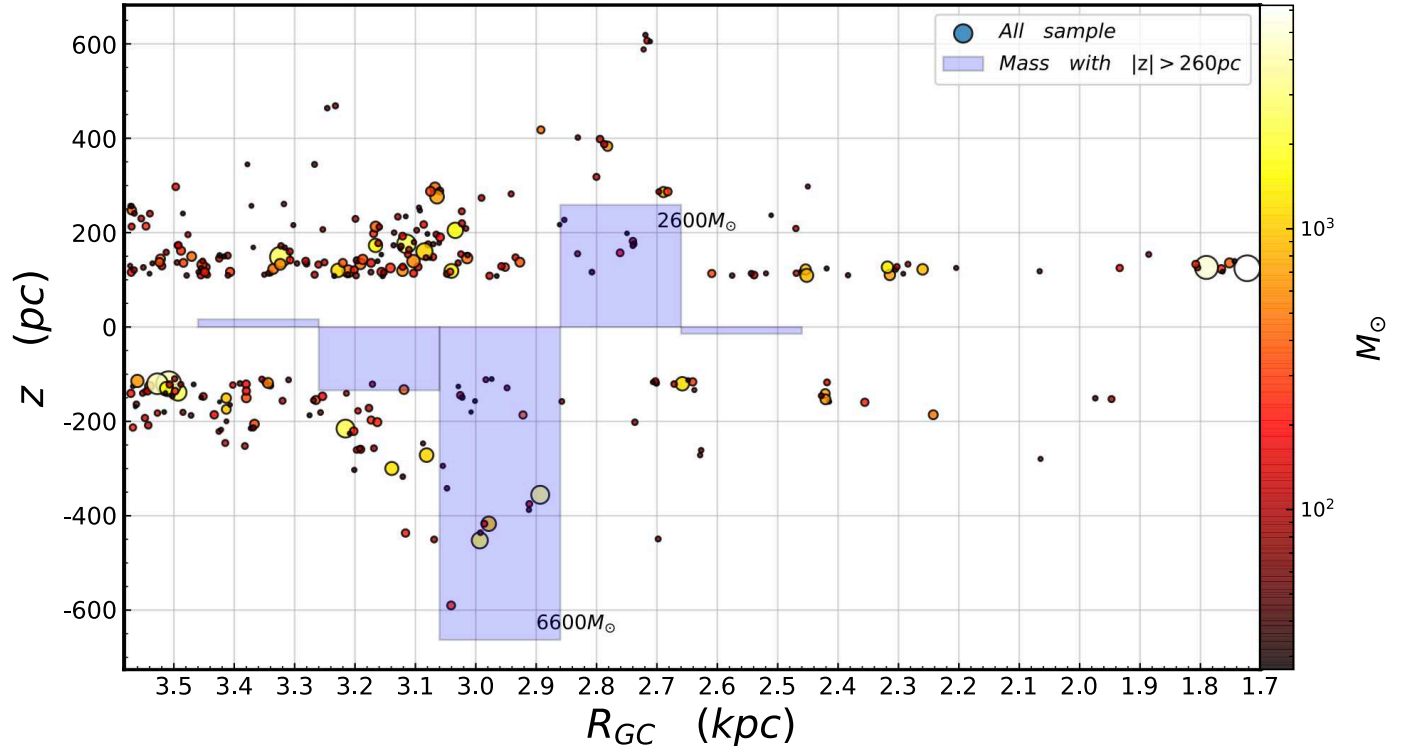


Figure 2. 321 high- z MCs in the R_{GC} - z map. The size of the filled circles is proportional to the effective radius of the MCs, while the color represents the mass of the clouds. The histogram shows the mass distribution of the MCs at $|z| \gtrsim 260$ pc (about $3 \times \text{FWHM}$ of the thin CO disk).

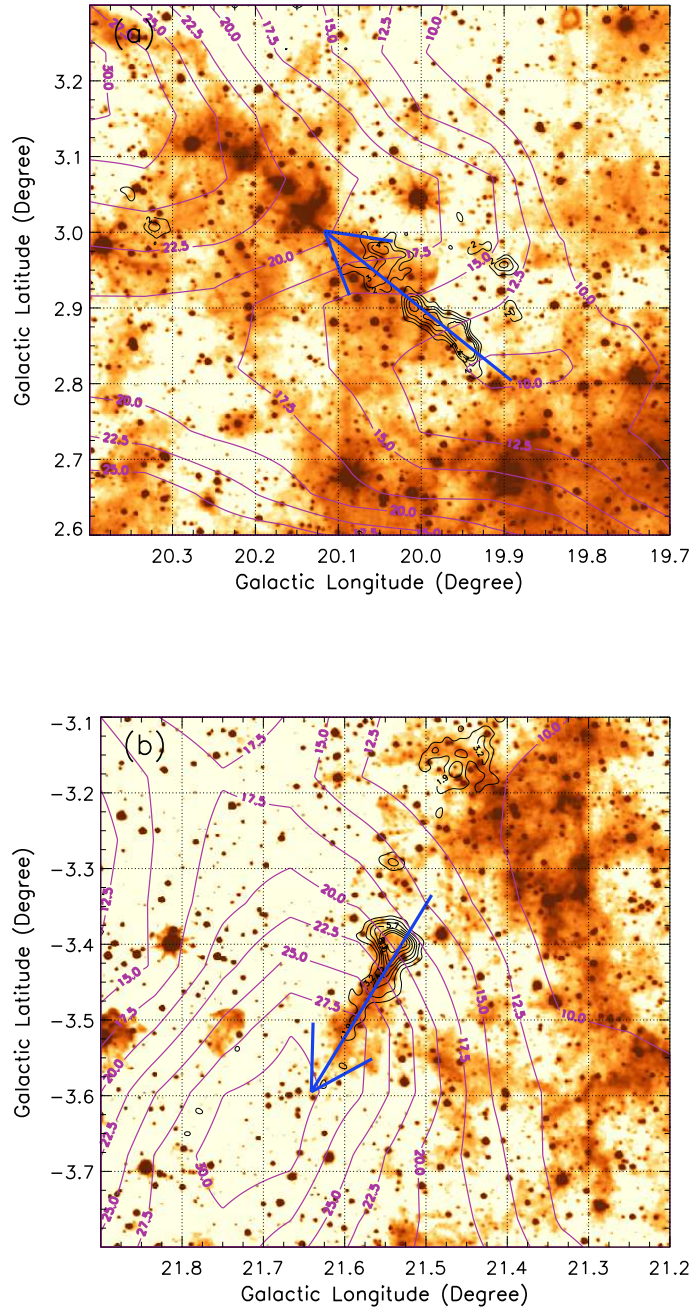


Figure 3. Multiwavelength views of two ELMCs toward the tangent points. The images display WISE 12 μm emission overlaid with the ^{12}CO integrated emission (black contours) and HI emission (purple contours) for the cometary clouds above (panel a for ELMC G019.957+02.863 in the velocity interval of 124–136 km s^{-1}) and below (panel b for ELMC G021.548–03.414 in the velocity interval of 114–125 km s^{-1}) the Galactic plane (see the red boxes in Figure 1). The blue arrows indicate the direction of the cometary structures from the head (toward the Galactic plane) to the tail. The PV diagrams along the arrows are shown in Figure 4.

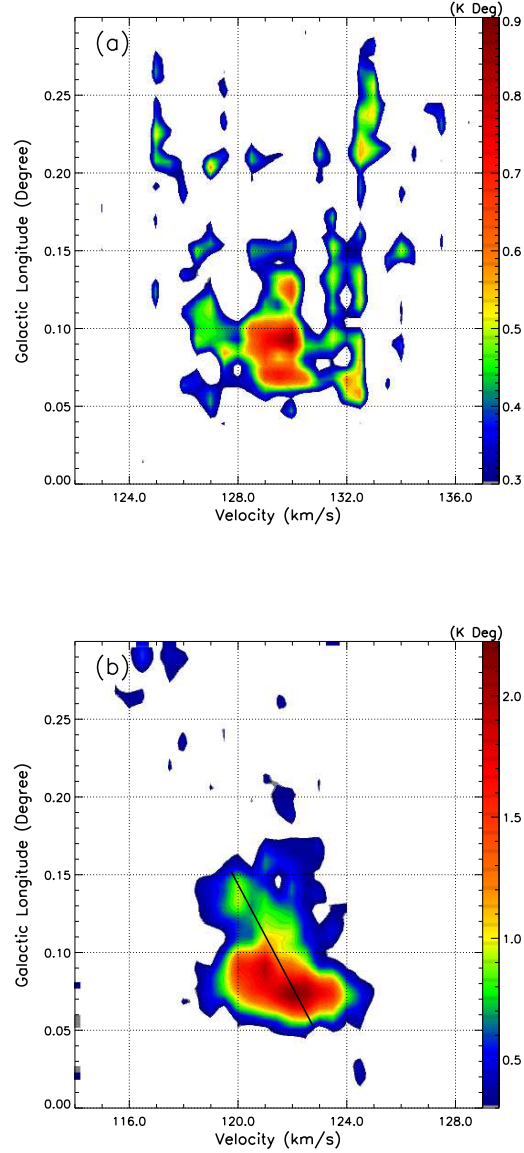


Figure 4. PV diagrams of the ^{12}CO emission of two EHMCs shown in Figure 3, i.e., panel (a) from ($l = 19^\circ 89$, $b = +2^\circ 80$) to ($l = 20^\circ 12$, $b = +3^\circ 00$) for EMMC G019.957+02.863, and panel (b) from ($l = 21^\circ 49$, $b = -3^\circ 34$) to ($l = 21^\circ 64$, $b = -3^\circ 60$) for EMMC G021.548-03.414. The two slices have a length of $0^\circ 3$ and a width of $3' 5$. The black line in panel (b) displays the velocity gradient of $\sim -0.23 \text{ km s}^{-1} \text{ pc}^{-1}$ at the tangent distance of ~ 7.6 kpc.

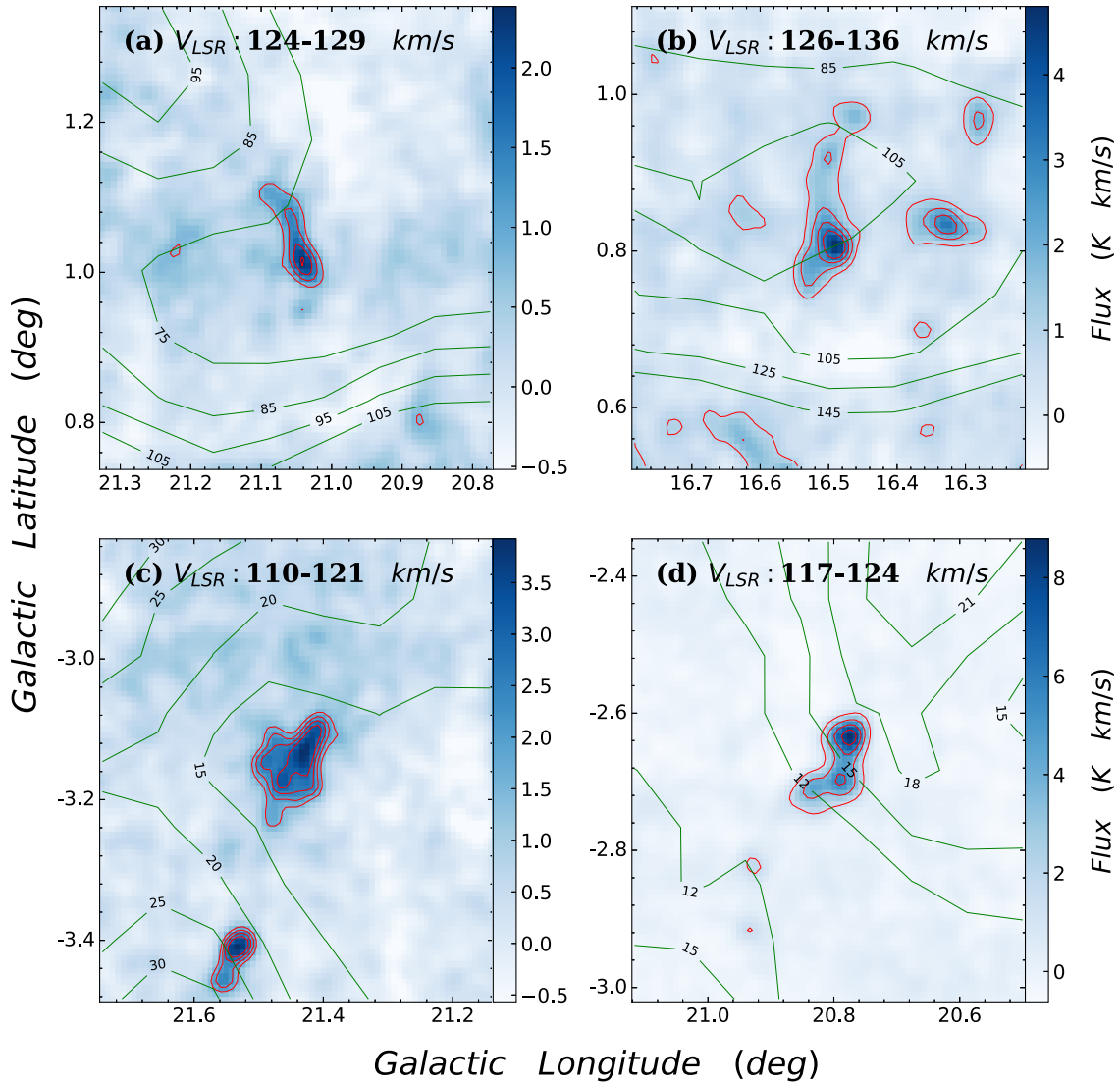


Figure 5. CO emission of four elongated high- z MCs, overlaid with the H I emission near the tangent points (green contours in units of $K \text{ km s}^{-1}$). The integrated velocity ranges of the CO emission are labeled in the upper left corner of each panel. The CO red contours are (a) 0.8, 1.3, 1.8, 2.3 $K \text{ km s}^{-1}$; (b) 1.0, 1.8, 2.6, 3.4 $K \text{ km s}^{-1}$; (c) 1.5, 2.0, 2.5, 3.0 $K \text{ km s}^{-1}$; and (d) 1.5, 3.5, 5.5, 7.5 $K \text{ km s}^{-1}$, respectively.

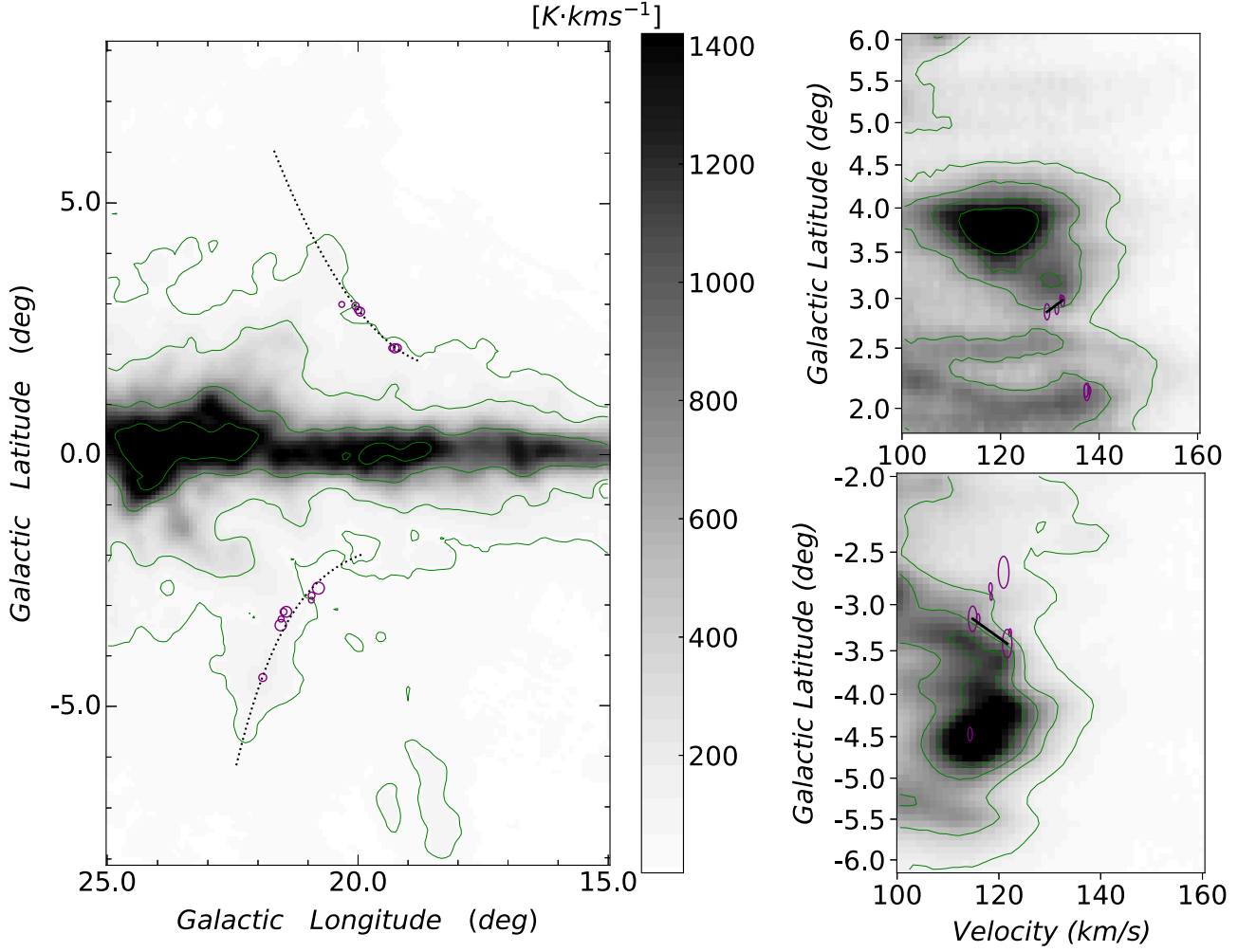


Figure 6. Left panel: HI intensity map overlaid with the EHMCS (purple circles) along the crater walls (black dashed lines). The green contours indicate the HI intensity of 50, 200, 800, and 1500 $K \text{ km s}^{-1}$ toward the tangent points. Top right panel: the PV diagram along the crater wall (with a width of $35'$) above the Galactic plane. The green contours are 0.6, 1.2, 1.8, and 2.4 K. The purple ellipses are the same EHMCS in the left panel (i.e., ID 5, 6, 7, 13, 14, 15, and 17 in Table 1). The black solid line indicates the velocity gradient of $\sim 0.15 \text{ km s}^{-1} \text{ pc}^{-1}$ for the coherent EHMCS. Bottom right panel: same as the top right panel, but for the crater wall below the plane. The green contours are 0.6, 1.8, 3.0, and 4.2 K. The purple ellipses are from Table 1 (ID 19, 20, 21, 23, 24, 26, 27, and 28). The velocity gradient is $\sim 0.16 \text{ km s}^{-1} \text{ pc}^{-1}$. Note that the EHMCS's size is not the true angular size of the detected CO emission, but it is proportional to the effective radius of the clouds.

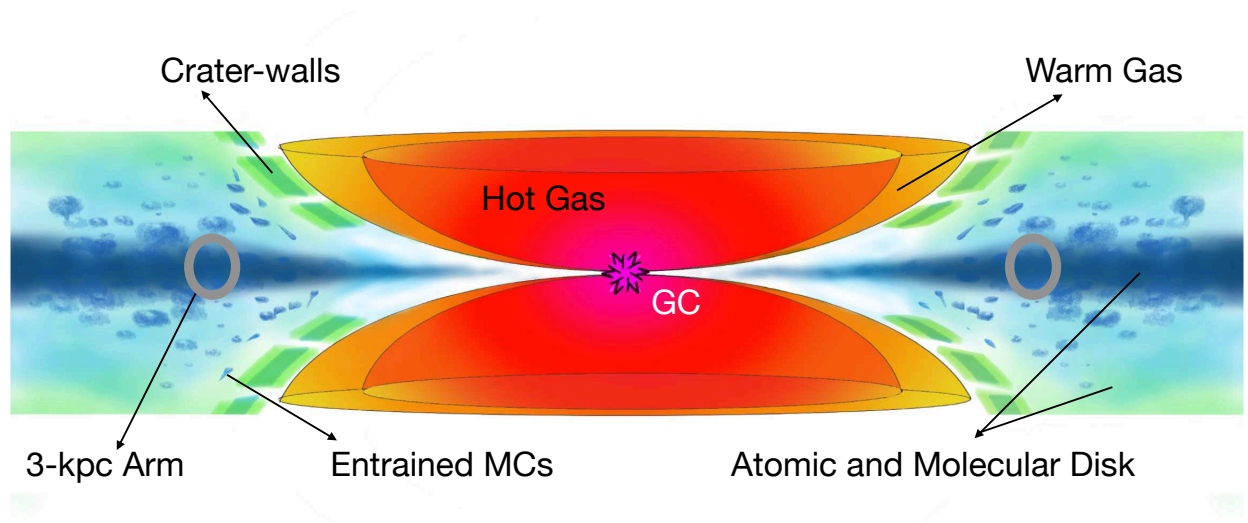


Figure 7. Schematic diagram of the relationship between the Milky Way nuclear wind and the gaseous disk (green is for the atomic gas, and blue is for the molecular gas). Note that the size of the MCs in the diagram is not exactly to scale because we aim to highlight the head-to-tail MCs pointing away from the Galactic plane. The same applies for the sizes of the crater walls.

Table 1. Parameters of 47 EHCs based on the MWISP $^{12}\text{CO}(J=1-0)$ Emission

ID	l	b	v_{LSR}	σ_v	T_{peak}	Radius ^a	Distance ^b	z Height	Mass	α^c
(1)	(deg)	(deg)	(km s^{-1})	(km s^{-1})	(K)	(pc)	(kpc)	(pc)	(M_{\odot})	(11)
01	14.675	-2.031	142.66	0.52	2.03	1.7	7.9	-280	71	7.6
02	17.495	2.194	141.26	0.67	1.72	1.7	7.8	298	76	11.6
03	18.803	-1.939	131.30	0.61	1.69	1.9	7.7	-261	70	11.7
04	18.815	-2.017	128.91	0.83	1.40	1.8	7.7	-272	75	19.1
05	19.214	2.135	137.37	1.24	1.62	3.5	7.7	287	322	19.4
06	19.267	2.129	137.53	2.35	1.93	4.6	7.7	286	789	37.6
07	19.324	2.135	138.05	1.04	1.85	2.1	7.7	287	120	22.3
08	19.332	-3.343	129.38	0.60	1.53	2.1	7.7	-449	74	12.2
09	19.430	4.502	129.72	0.97	1.32	1.4	7.7	605	53	28.9
10	19.468	4.515	128.17	1.25	2.05	2.6	7.7	607	153	30.8
11	19.489	4.605	129.97	0.81	1.53	1.8	7.7	619	58	23.7
12	19.512	4.378	137.76	0.73	2.08	1.8	7.7	588	104	10.7
13	19.957	2.863	129.44	1.63	1.88	4.2	7.7	383	620	21.0
14	19.999	2.897	131.42	0.91	1.52	2.9	7.7	388	139	19.9
15	20.051	2.978	132.61	0.64	1.30	2.9	7.7	398	107	13.1
16	20.095	2.380	124.45	1.07	1.67	2.6	7.7	318	133	26.4
17	20.326	3.007	132.28	0.71	1.64	1.9	7.6	402	65	17.1
18	20.785	3.138	115.74	1.58	1.93	3.1	7.6	418	466	19.4
19	20.794	-2.672	120.93	1.27	4.61/1.26 ^d	8.1	7.6	-356	3118	4.9
20	20.930	-2.821	118.36	0.67	1.36	2.6	7.6	-375	128	10.2
21	20.934	-2.914	118.50	0.65	1.82	1.8	7.6	-388	75	11.7
22	21.156	2.125	114.33	0.90	1.61	2.2	7.6	282	103	20.2
23	21.436	-3.146	114.85	1.84	1.78	6.5	7.6	-417	1012	25.4
24	21.491	-3.147	115.91	1.39	1.32	2.6	7.6	-417	170	34.3
25	21.526	2.067	137.91	0.95	1.17	2.5	7.6	274	101	26.3
26	21.540	-3.291	122.20	0.98	1.43	2.0	7.6	-436	108	20.5
27	21.548	-3.414	121.63	1.39	4.36/1.14 ^d	7.2	7.6	-452	2340	7.0
28	21.908	-4.462	114.33	0.92	2.72	3.5	7.6	-590	281	12.3
29	21.959	-2.589	125.82	0.77	1.59	1.9	7.6	-342	73	17.6
30	22.011	-2.231	114.55	0.71	1.45	1.8	7.6	-294	71	14.4
31	22.050	2.185	128.01	0.45	1.20	3.0	7.6	288	80	8.9
32	22.085	2.095	130.88	0.86	2.34	6.2	7.6	276	685	7.7
33	22.110	2.242	127.66	1.30	2.03	4.5	7.6	296	443	20.1
34	22.121	-3.413	116.77	0.56	1.49	2.5	7.6	-450	102	9.1
35	22.166	2.181	131.57	0.71	2.15	4.0	7.5	288	316	7.5
36	22.216	-2.061	113.76	1.64	2.18	6.1	7.5	-272	1114	17.0
37	22.481	-3.318	115.78	0.69	2.12	3.2	7.5	-437	231	7.8
38	22.515	-2.412	111.25	0.68	1.18	1.9	7.5	-317	44	22.7
39	22.654	-2.283	111.06	1.75	2.32	5.8	7.5	-300	1262	16.4
40	23.098	-1.990	125.68	1.30	1.86	2.4	7.5	-261	113	42.1
41	23.128	-2.314	121.09	0.47	1.14	1.8	7.5	-303	38	11.7
42	23.367	3.585	117.59	0.58	1.24	2.2	7.5	469	68	12.5
43	23.470	3.550	115.42	0.44	1.54	1.9	7.5	464	50	8.2
44	23.632	2.642	111.06	0.75	1.00	2.1	7.5	345	54	25.3
45	24.021	2.006	121.30	0.55	1.51	1.9	7.4	261	66	9.9
46	24.488	2.661	109.69	0.36	1.67	1.5	7.4	345	43	5.3
47	25.408	2.311	108.45	1.31	1.57	2.8	7.4	297	193	29.1

NOTE— ^a The effective radius of the clouds. ^b The error of the estimated distance is about 2%–20% assuming that the MCs are located near tangent points with a velocity uncertainty of $\sim 5 \text{ km s}^{-1}$ along the line of sight (see, e.g., the A5 model in Reid et al. 2019). ^c The MC’s virial parameter estimated from the definition of $\alpha = \frac{5\sigma_v^2 R}{GM_{\text{Xfactor}}}$ (see Section 3.3). ^d Detected ^{13}CO emission associated with ^{12}CO emission. The ^{13}CO emission is very weak, i.e., $T_{\text{peak}13} \sim 1 \text{ K}$.